Civil Engineering and Applied Solutions

Research Article

journal homepage: ceas.journals.umz.ac.ir

CEAS Civil Engineering and Applied Solutions

A Data-Driven Seismic Design Framework for RC Frames Using Wavelet Transforms and Machine Learning

Sina Farahani [a*]

[a] *Department of Civil Engineering, Faculty of Civil Engineering and Architecture, Shahid Chamran University of Ahvaz, Ahvaz, Iran*

ARTICLE INFO

Article history:

Received 12 January 2026

Revised 13 February 2026

Accepted 07 May 2026

Available online 01 January 2027

Keywords:

Reinforced concrete moment resisting frame

Wavelet transform

Machine learning-based method

Seismic behavior

Dynamic analysis

ABSTRACT

Nowadays, reinforced concrete (RC) frames are one of the most well-developed lateral load-resisting systems used around the world. However, the complex nonlinear behavior of the composite material system, which combines steel and concrete, makes precise seismic analysis and design particularly challenging. Established methods, such as modal response history analysis and time history analysis, are often difficult to apply. This challenge is compounded when significant soil-structure interaction alters the structural response through higher mode effects. Consequently, the development of innovative analytical methods that are both simplified and robust remains a primary challenge in advancing the design of these structural systems. This study presents a novel wavelet transform-based machine learning method (WTMLM) for the seismic design of RC frames. The method incorporates soil-structure interaction (SSI) effects and formulates the dynamic equilibrium of the system. The proposed WTMLM is used to design five RC frames with varying story heights on two different soil types. The performance is evaluated using nonlinear time-history analyses (NTHA) under real ground motions. Finally, a new equation for predicting displacement distribution is developed based on machine learning and median NTHA results. The findings indicate the WTMLM is an effective method for controlling the seismic performance of RC structures.

How to cite this article: Farahani, S. A Data-Driven Seismic Design Framework for RC Frames Using Wavelet Transforms and Machine Learning. Civil Engineering and Applied Solutions. 2027; 3(1): 1–24. doi:10.22080/ceas.2026.30950.1073.

1. Introduction

The global impact of earthquakes presents a profound risk to human safety, critical infrastructure, and economic systems. These seismic events induce vibrations that generate internal forces and displacements in reinforced concrete (RC) structures. Crucially, at the ultimate nonlinear performance level, the resulting structural damage is a function of the displacement history at each degree of freedom (DOF). Determining this damage precisely requires solving the structural response via exact dynamic equilibrium equations, which in turn necessitates a complete time history of the ground motion-induced forces. However, the vibration characteristics of earthquake signals are non-harmonic and highly unpredictable, making such a precise analysis challenging. Furthermore, employing exact methods such as nonlinear time-history analysis (NTHA) and modal response history analysis (MRHA) in the initial design phase is complex and time-consuming. Moreover, incorporating soil-structure interaction (SSI) into the analysis introduces additional degrees of freedom and leads to a more complex formulation of the coupled equations of motion. This added complexity further exacerbates the challenges of precise seismic assessment. Consequently, major design codes, such as ASCE 7-22 [1], Eurocode 8 [2], and the Iranian Standard 2800 [3], provide simplified methods like the Equivalent Lateral Force (ELF) procedure. Although the ELF procedure simplifies the design process by primarily considering the fundamental mode of vibration, it omits the time-dependent characteristics of seismic motion and the complexities introduced by SSI. This simplification

* Corresponding author.
E-mail addresses: s.farahani@scu.ac.ir (S. Farahani).

https://doi.org/10.22080/ceas.2026.30950.1073
ISSN: 3092-7749/

can lead to an underestimation of story shears, particularly in the upper levels of a structure, due to the influence of higher-mode effects.

Conversely, solving the equation of motion is significantly simplified when the excitation can be represented by a periodic harmonic force, as this permits a precise analytical solution [4]. Furthermore, research has demonstrated that displacement has a greater influence on structural performance than resistance during seismic events [4-7]. Consequently, displacement can be considered a critical parameter for controlling structural damage. This understanding has led the field of seismic design to increasingly adopt displacement-based methods. Within this framework, the accurate estimation of seismic-induced damage is achieved by treating displacement as a fundamental performance parameter. In essence, a method that successfully incorporates displacement as a key parameter and represents the seismic excitation with an equivalent periodic harmonic force would yield a more efficient solution to the dynamic equation of motion and a more accurate prediction of the structural response [8, 9].

Recently, robust signal processing methods, such as those based on wavelet transform and machine learning (ML), have been applied to predict seismic performance corresponding to equivalent forces in practical applications. Imam et al. [10] demonstrated the practical application of machine learning for seismic performance prediction of steel frames. By training models like Random Forest and XGBoost on a large dataset generated from nonlinear dynamic analyses, they achieved highly accurate predictions of maximum inter-story drift and corresponding damages. Demir et al. [11] highlighted a critical success factor for ML in engineering, demonstrating that feature selection and data cleaning significantly enhance model performance, with Random Forest consistently emerging as the most robust predictor. Farahani and Barari [12] developed an ML-based model using the Group Method of Data Handling (GMDH) that accounts for the complex interplay of multiple displacement properties in offshore structures. The wavelet transforms have been successfully applied to various challenges in structural engineering, including signal processing of ground motions, damage detection, and simplifying complex dynamic analyses. The potential of wavelet transforms to tackle computational cost in seismic design was recognized early on. For instance, Salajegheh et al. [13] demonstrated over a decade ago that the Discrete Wavelet Transform could drastically reduce the number of points in an earthquake record, enabling a much faster optimization process for structural weight. Kamgar et al. [14] provided a crucial insight into the practicality of wavelet transforms, establishing that the first-level approximation of a decomposed seismic signal could predict key SSI response parameters with over 90% accuracy, offering a compelling balance between computational efficiency and precision. Dadkhah et al. [15] quantified a highly favorable trade-off between efficiency and precision in seismic analysis. Their work showed that applying DWT to filter ground motions for IDA slashes computational effort by nearly 87% while maintaining a maximum error below 8%, a compromise that is acceptable for many engineering applications. A compelling precedent for using signal processing to simplify complex analyses was set by Kamgar et al. [16], who demonstrated that the Discrete Wavelet Transform (DWT) could reduce the computational time of nonlinear dynamic analysis while maintaining acceptable accuracy. Yang et al. [17] used experiments to prove that wavelet analysis works for soil-structure interaction problems. Their real-world test results provide a strong foundation for data-driven models like the one in this study. The trend toward intelligent, self-adjusting structural systems is exemplified by the work of Zhang et al. [18]. They created a semi-active damper that uses an LSTM-Wavelet algorithm to dynamically retune itself, proving highly effective for retrofitting aging structures with degraded stiffness.

In parallel with the development of signal-based seismic design methodologies, significant advances have been made in modeling soil and foundation response under dynamic loading. Asgari and Bagheripour [19] employed the Hybrid Frequency Time Domain (HFTD) approach to evaluate nonlinear ground response. They demonstrated that iterative frequency–time domain coupling can efficiently capture strain-dependent soil behavior, a concept relevant to the equivalent linear soil representation adopted in the present study. The influence of soil liquefaction and multi-hazard loading on pile-supported systems has also been extensively investigated. Akbarzadeh et al. [20] examined offshore wind turbines on liquefiable soils, while Asgari et al. [21] studied pile groups in laterally spreading soils. Both studies highlighted the critical role of soil–structure interaction, frequency content, and pile configuration in overall system performance. More recently, Asgari and Ahmadtabar Sorkhi [22] developed parameterized fragility and sensitivity frameworks that quantify the influence of uncertain mechanical and geotechnical parameters on structural vulnerability. Their work emphasizes the need for data-driven approaches that can account for such uncertainties. While the present study focuses on wavelet-based pulse generation and machine learning-assisted design, the broader body of research on nonlinear soil response, SSI, and uncertainty quantification provides both theoretical grounding and motivation for the proposed WTMLM framework. Regarding the choice of time–frequency analysis tool, the wavelet transform was selected for its well-established capability to capture non-stationary frequency content of earthquake records while maintaining temporal localization. However, alternative transforms such as the Stockwell Transform offer distinct advantages, including absolute phase preservation and frequency-dependent spectral localization, which can enhance interpretability and stability for certain classes of seismic signals [21, 22]. A comparative evaluation of wavelet-based and S-Transform-based pulse generation within the WTMLM framework is beyond the scope of the present study, but is acknowledged as a valuable direction for future refinement.

This study introduces a novel Wavelet Transform-based Machine Learning Method (WTMLM) for the seismic design of reinforced concrete (RC) frames. The primary innovation of this study lies in the novel integration of wavelet transforms and machine learning to generate equivalent pulse functions directly from recorded ground motions. This represents a departure from existing methods that rely on idealized pulse shapes or equivalent oscillators. The proposed approach preserves the non-stationary frequency content of real earthquakes and, for the first time, embeds SSI effects within a data-driven design framework validated through rigorous nonlinear analysis. The proposed methodology begins by utilizing the wavelet transform to decompose a selected set of ground motions into two distinct levels. The WTMLM is subsequently developed by employing a shear beam model, formulating the dynamic equilibrium of the structure, and correcting the mass, stiffness, and damping matrices. A key innovation

of this approach is the replacement of the force term in the equation of motion with an equivalent pulse function. To achieve this, the study proposes a new solution that converts real earthquake records into a representative pulse function using wavelet transformation. This process introduces a pulsed sine function to generate equivalent seismic forces by filtering out frequency content that falls outside the critical design range. Subsequently, the WTMLM is applied to design five RC frames of 3, 6, 9, 12, and 15 stories, considering two different soil conditions. The seismic performance of these designed frames is then rigorously evaluated using Nonlinear Time History Analysis (NTHA) to verify that they achieve the target performance level. Finally, leveraging the median maximum-story displacements derived from the NTHA results, a machine learning-based predictive equation is formulated for the displacement prediction of RC frames, explicitly accounting for soil-structure interaction (SSI) effects.

2. Development of wavelet transform-based machine learning method (WTMLM)

2.1. Equivalent SDOF system substitution

In the initial step, the main structure is idealized as a single-degree-of-freedom (SDOF) system characterized by an equivalent mass and an effective height. Based on a target performance level and the corresponding demand displacement, the displacement prediction formula of the RC structure is determined using Eq. 4 [4, 5]. Once the demand displacement is established, the effective period of the structure is obtained from the displacement response spectrum of the seismic-prone area for the considered earthquake scenario. Using this effective period, Eqs. 1 to 3 are subsequently applied to calculate the effective stiffness, the base shear, and the distribution of lateral forces over the height of the structure.

$$K_e = 4\pi^2 \frac{m_e}{T_e^2} \tag{1}$$

$$V_b = K_e \Delta_d + C \frac{m_e g \Delta_d}{H_e} \tag{2}$$

$$F_i = \frac{m_i \Delta_i}{\sum m_i \Delta_i} V_b \tag{3}$$

In Eq. 2, the second term accounts for the P-Delta effect. The effective height H_e, effective mass m_e, and demand displacement Δ_d in the equations above are determined by Eqs. 4 to 6 as follows:

$$\Delta_d = \frac{\sum m_i {\Delta_i}^2}{\sum m_i \Delta_i} \tag{4}$$

$$m_e = \frac{\sum m_i \Delta_i}{\Delta_d} \tag{5}$$

$$H_e = \frac{\sum m_i \Delta_i h_i}{\sum m_i \Delta_i} \tag{6}$$

Which are in Eqs. 4 to 6, Δ_i, m_i and h_i, the design displacement of RC structures, seismic mass, and height in the i level, respectively.

2.2. The formulation of the model includes degrees of freedom representative of SSI

The shear beam model, originally proposed by Idriss Izzat and Seed [23] for multilayer soil, is adopted in this study to develop the WTMLM. This formulation focuses on the translational degrees of freedom of the soil-structure system. While this approach captures the essential coupling between soil flexibility and structural lateral response, it intentionally excludes the rocking degree of freedom of the foundation. This simplification is justified for the scope of this study, which involves low- to mid-rise RC frames with squat configurations on relatively stiff soil, where translational SSI effects dominate the global seismic response [4, 9]. As depicted in Fig. 1, this model idealizes the soil as an n-degree-of-freedom (DOF) system, where each DOF possesses unique stiffness and damping properties. This multi-layered representation is well-suited for evaluating the realistic behavior of soil. Each soil layer is substituted with a concentrated mass m_i and stiffness K_i, according to Eqs. 7 and 8.

$$m_i = \frac{\gamma_{i-1} h_{i-1} + \gamma_i h_i}{g} \tag{7}$$

$$K_i = {G_i}/{2h_i} \tag{8}$$

In Eqs. 7 and 8, G_i is the shear modulus of the soil layer. Also h_i and h_{i-1} are the half-thicknesses of soil layers i and $i-1$, respectively. However, m_1 is a lumped mass placed at the top of soil layer 1, which is calculated just using the half thickness of soil layer 1(h_1).

Moreover, the initial slope correction method is used to evaluate the effects of the material nonlinearity of soil [24]. Based on this method, the non-linear behavior of the real soil is replaced by an equivalent linear model. This linear model will be used to solve the dynamic equilibrium equation by the MODAL method in section 5. As shown in Fig. 2, in the slope correction method, the initial slope G_0 of the shear stress-shear strain curve in the linear region will be modified by the use of a decreasing factor, namely, the seismic hazard area coefficient N_0, for evaluating nonlinear effects. In Eq. 9, the coefficient N_0 is obtained from FEMA440 [24] illustrated in Table 1. Hence, by the use of this approach, the nonlinear effects of the soil can be obtained in an equivalent linear way employing Eqs. 9 and 10 as follows:

$$G_i = N_0 G_0 (^{\text{ton}}/_{\text{m}^2}) \quad (9)$$

$$G_0 = \frac{\gamma}{g} V_s^{\,2} (^{\text{ton}}/_{\text{m}^2}) \quad (10)$$

In Eq. 10, γ and V_s are the specific weight and shear wave velocity of the soil layer, respectively.

Fig. 1. Conceptual shear beam model for multi-layered soil.

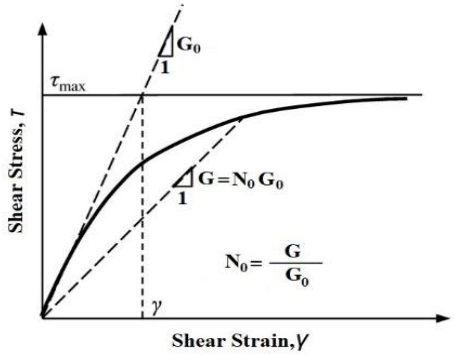

Fig. 2. Modified soil behavior model.

Table 1. The values of the shear modulus ratio [24].

PGA(g)	≤ 0 · 10	0 · 15	0 · 20	≥ 0 · 30
Value of $N_0 = G/G_0$	0.81	0.64	0.49	0.42

2.3. Displacement profile of RC frame

The displacement profile of the moment-resistant RC frame is obtained by Eq. 11, taking into account its ideal mechanism, defined as plastic hinges formed at the end of the beams and base of the columns using the strong column-weak beam concept [7]:

$$\Delta_{i.RC} = \theta_c h_i \left[\frac{4h_n - h_i}{4h_n - h_1}\right] \quad (11)$$

In the above equation, θ_c is drift ratio is calculated with regard to the performance level based on the damage to the structural or non-structural members. Moreover, the design displacement profile of the RC frame is modified upon Eq. 12, given as follows:

$$\Delta_{i.SYS} = \omega_\theta (\theta_c h_i \left[\frac{4h_n - h_i}{4h_n - h_1}\right]) \quad (12)$$

The coefficient ω_θ is a modification factor of the higher mode effects obtained by Eq. 13 [7]:

$$\omega_\theta = 1 \cdot 15 - 0 \cdot 0034 h_n \leq 1 \quad (13)$$

2.4. Final characteristics of the SDOF system

In the following, the characteristics of the equivalent SDOF system are calculated:

$$\Delta_d = \frac{\sum_{i=1}^{n} (m_i \cdot \Delta_{i.SYS}^{\,2})}{\sum_{i=1}^{n} (m_i \cdot \Delta_{i.SYS})} \quad (14)$$

$$H_e = \frac{\sum_{i=1}^{n} (m_i \cdot \Delta_{i.SYS} \cdot h_i)}{\sum_{i=1}^{n} (m_i \cdot \Delta_{i.SYS})} \quad (15)$$

$$m_e = \frac{\sum_{i=1}^{n} (m_i \cdot \Delta_{i.SYS})}{\Delta_d} \quad (16)$$

In these equations, the characteristics of the SDOF system are Δ_d H_e, m_e named as displacement demand, effective height, and effective mass, respectively. To modify the displacement design profile for the desired damping level, the yield displacement of the RC frame system ($\Delta_{y.RC}$) is first obtained from Eqs. 17 to 19 [5].

$$\Delta_{y.RC} = \theta_{y.RC} \cdot H_e \quad (17)$$

$$\theta_{y.RC} = 0 \cdot 5 \cdot \varepsilon_y \cdot \frac{L_b}{h_b} \quad (18)$$

$$\Delta_{y.RC-system} = [0 \cdot 5 \cdot \varepsilon_y \cdot \frac{L_b}{h_b} \cdot H_e] \quad (19)$$

In the equations above, $\theta_{y.RC}$, L_b, and h_b represent the yield drift ratio, span length, and depth of the beam, respectively. At this stage, with both Δ_d and $\Delta_{y.RC}$ known, Eq. 20 is used to determine the demand ductility:

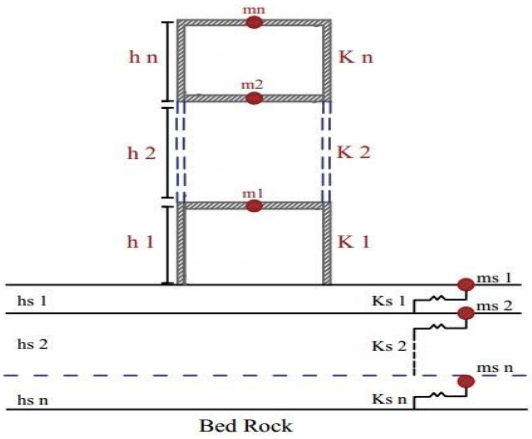

Fig. 3. Numerical model developed in this study.

$$\mu_{RC} = \frac{\Delta_d}{\Delta_{y.RC-system}} \quad (20)$$

The equivalent viscous damping of the system is calculated using Eq. 21.

$$\xi_{eq.RC} = 0 \cdot 05 + 0 \cdot 565(\frac{\mu_{RC} - 1}{\mu_{RC} \cdot \pi}) \quad (21)$$

In the next step, Eq. 22 is used to determine the modification damping factor of the displacement profile.

$$R_\xi = (\frac{0 \cdot 07}{0 \cdot 02 + \xi_{eq.RC}})^{0 \cdot 5} \quad (22)$$

Moreover, Eq. 23 is proposed to obtain the viscous damping coefficient.

$$C_e = 2 \cdot \xi_{eq.RC} \cdot (\frac{2\pi}{T_e})^2 \quad (23)$$

2.5. Development of a three-degree-of-freedom system

This stage involves extending the SDOF equivalent system from subsection 2.1 to a multi-degree-of-freedom (MDOF) system. The proposed MDOF model, illustrated in Fig. 3, represents an N-degree-of-freedom system that integrates both the N-story structure and the different soil layers. The dynamic equilibrium equation for a multi-degree-of-freedom (MDOF) system excited by external vibration forces P(t) is typically presented in the following form [8]:

$$[M]\{\ddot{u}\} + [C]\{\dot{u}\} + [K]\{u\} = \{P(t)\} \quad (24)$$

Prior to composing and solving the equilibrium Eq. 24, the constituent matrices, including the mass, stiffness, and damping matrices and the force vector, must be extended to include SSI effects. In this study, the shear beam model of SSI with two distinct soil layers is utilized to extend the matrices of the dynamic equilibrium equation. To this end, the SDOF equivalent system is first modified into a three-degree-of-freedom (3DOF) system by incorporating two additional DOFs representing the two soil layers, as illustrated in Fig. 4. The mass, stiffness, and damping matrices for the proposed three-degree-of-freedom equivalent system are developed using Eqs. 25 through 27. These matrices are three-by-three square matrices. The first degree of freedom corresponds to the equivalent SDOF of the structure, characterized by its effective mass (m_e), effective damping (C_e), and effective stiffness (K_e).

The remaining two degrees of freedom are assigned to the soil layers, each characterized by its mass, damping, and stiffness (m_{si}, C_{si}, and K_{si}), where i denotes the layer number. As illustrated in these equations, the matrix components in the present formulation are fundamentally different from those extended in Lu et al. [25]. For instance, unlike their formulation, the mass matrix in Eq. 25 does not incorporate rotational inertia. Furthermore, the equivalent structural mass (m_e) is determined using Eq. 16, while the concentrated soil masses ($m_{s1}.m_{s2}$) are calculated for each layer using Eq. 7. Similar to the impedance model in Lu et al. [25], the proposed stiffness matrix in Eq. 26 differs by excluding a rotational stiffness term. Furthermore, its components are ordered according to the stiffness of each respective soil layer. The matrix components for the soil layers and the superstructure are calculated using Eqs. 1 and 8, respectively. For the damping matrix in Eq. 27, the equivalent structural damping is determined from Eq. 23,

while the damping terms for the soil layers are modeled using the Rayleigh damping method. In general, as depicted in Fig. 4, this proposed three-degree-of-freedom system provides a more accurate numerical model than an SDOF system.

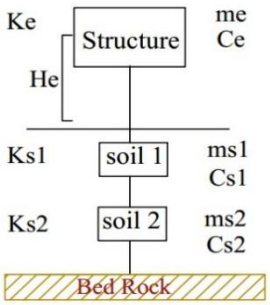

Fig. 4. Proposed 3-degree-of-freedom model in the current study.

$$[M] = \begin{bmatrix} m_e & 0 & 0 \\ 0 & m_{s1} & 0 \\ 0 & 0 & m_{s2} \end{bmatrix} \tag{25}$$

$$[k] = \begin{bmatrix} \mathrm{K_e} & -\mathrm{K_e} & 0 \\ -\mathrm{K_e} & \mathrm{K_{s1}} + \mathrm{K_e} & -\mathrm{K_{s1}} \\ 0 & -\mathrm{K_{s1}} & \mathrm{K_{s1}} + \mathrm{K_{s2}} \end{bmatrix} \tag{26}$$

$$[c] = \begin{bmatrix} C_e & -C_e & 0 \\ -C_e & C_{s1} + C_e & -C_{s1} \\ 0 & -C_{s1} & C_{s1} + C_{s2} \end{bmatrix} \tag{27}$$

Finally, the dynamic equilibrium equation of the proposed 3-degree-of-freedom system is presented as follows:

$$\begin{bmatrix} m_e & 0 & 0 \\ 0 & m_{s1} & 0 \\ 0 & 0 & m_{s2} \end{bmatrix} \{\ddot{u}\} + \begin{bmatrix} C_e & -C_e & 0 \\ -C_e & C_{s1} + C_e & -C_{s1} \\ 0 & -C_{s1} & C_{s1} + C_{s2} \end{bmatrix} \{\dot{u}\} + \begin{bmatrix} \mathrm{K_e} & -\mathrm{K_e} & 0 \\ -\mathrm{K_e} & \mathrm{K_{s1}} + \mathrm{K_e} & -\mathrm{K_{s1}} \\ 0 & -\mathrm{K_{s1}} & \mathrm{K_{s1}} + \mathrm{K_{s2}} \end{bmatrix} \{u\} = \{P(t)\} \tag{28}$$

It is important to note that this study aims to generate a closed-form equation by theoretically solving the dynamic equilibrium equation (i.e., Eq. 28). Consequently, the force vector {P(t)} on the right-hand side of Eq. 28 must be replaced with equivalent force functions to facilitate modal analysis and solve the system of equations, leading to the development of uncoupled equations of motion. To this end, the WTMLM is proposed in the next subsection to generate the required equivalent force function.

2.6. Frequency band separation and equivalent force generation via WTMLM

Seismic data from past earthquakes are typically available as acceleration time histories. However, these records are often of short duration and exhibit significant dispersion, making them unsuitable for deriving theoretical, closed-form solutions required for seismic analysis of the system. While solving the dynamic equilibrium equation is essential for this derivation, the irregular nature of real ground motions complicates analysis and prevents a closed-form solution. Similarly, MRHA is also inadequate, as it does not yield a closed-form solution [8]. As an alternative, this study proposes the use of an equivalent pulse signal, generated via WTMLM, to replace the real earthquake record in the analytical development. These equivalent pulse signals are well-defined mathematical functions. Consequently, they can be substituted for the force vector {P(t)} on the right-hand side of the dynamic equilibrium equation, enabling a theoretical solution. Previous studies indicate that earthquake records comprise distinct high- and low-frequency bands. While the high-frequency components often contain the peak accelerations, their most significant impact occurs near the structure's fundamental period due to resonance. Consequently, an equivalent pulse function can be suitable for developing theoretical equations, provided it is defined to accurately represent these influential frequency bands. This approach of substituting real seismic signals with equivalent pulses has gained scholarly interest in recent decades. For instance, Agrawal and He [26] proposed Eq. 29, which models the equivalent pulse using a decaying sinusoidal function.

$$\dot{u}_g = s \times e^{-\zeta_p \omega_p t} \sin\left(\omega_p \sqrt{1 - {\zeta_p}^2} \cdot t\right) \tag{29}$$

This equation was derived by fitting a curve to the approximate maximum velocity response in the velocity-time history of the earthquake. The corresponding acceleration signal is subsequently obtained by differentiating Eq. 29. Similarly, Makris and Black [27] introduced two functions, presented as Eqs. 30 and 31 and designated Type A and Type B, respectively, to model equivalent pulses. These functions calculate the acceleration signal using sine and cosine formulations. In both equations, the amplitude parameter (v_p) represents the maximum pulse velocity, determined by fitting the velocity functions to their peak value.

$$\ddot{u}_g = \omega_p \frac{v_p}{2} sin\ (\omega_p t) \tag{30}$$

$$\ddot{u}_g = \omega_p v_p cos\ (\omega_p t) \tag{31}$$

Amiri et al. [28] evaluated the three pulse functions defined by Eqs. 29 to 31. Their findings indicate that while Eqs. 29 and 30 yield more accurate results than Eq. 31; time-history analyses reveal significant discrepancies between the responses from these equivalent pulses and those from real earthquake records. This inherent variability constitutes a major drawback, reducing the

precision of numerical simulations. To overcome these limitations, the current study introduces a novel method for generating a pulse function from a real earthquake record by employing the wavelet transform. The wavelet transform is uniquely suited for this task because it can accurately capture the time-varying frequency content of seismic signals. It is a highly efficient mathematical tool for signal processing, developed to overcome the limitations of the Fourier transform. While knowledge of a signal's frequency content can reduce error in the structural response, the Fourier transform is restricted by its use of constant-duration time windows, which limit its analysis of transient signals. In contrast, the wavelet transform employs variable time windows, allowing it to adaptively resolve frequency components at any point in time [29]. This provides a more accurate representation of non-stationary signals like earthquake records. The current study employs the wavelet transform to generate an equivalent pulse signal for earthquakes, as it effectively captures their time-varying frequency content. This is achieved by isolating the critical frequency bands within the hazardous range of the real seismic signals. As illustrated in Fig. 5a, the original signal is decomposed into wavelets across variable frequency bands. Using an ML-based algorithm in MATLAB, each earthquake record is decomposed into approximate (low-frequency) and detail (high-frequency) wavelet components. Indeed, an ML-based algorithm is applied to each decomposed wavelet component. A candidate pool of pulse functions, including sinusoidal, exponentially damped, and wavelet-based analytical forms, is evaluated against the reconstructed signal segment. The algorithm selects the function and optimizes its parameters, such as amplitude, frequency, and phase shift, to minimize the Square-Root-of-Sum-of-Squares (SRSS) error between the fitted pulse and the target wavelet. This process is repeated across all significant duration segments, and the optimal pulse family is retained for each ground motion. The training data for this phase consist of the decomposed wavelet coefficients themselves, and no separate validation set is required as the error metric is computed directly on the signal being modeled.

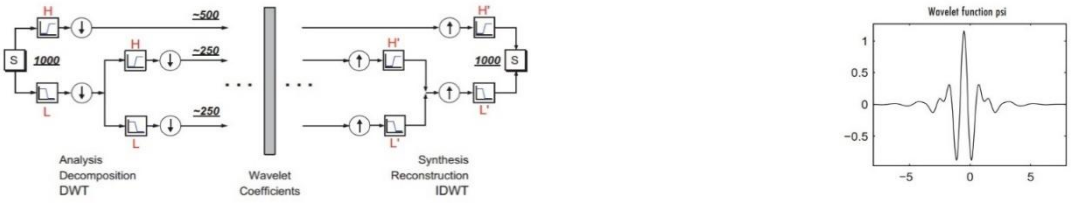

(a) **(b)**

Fig. 5. Wavelet transform of the primary signal: (a) wavelet decomposition and reconstruction steps, (b) Meyer wavelet function [29].

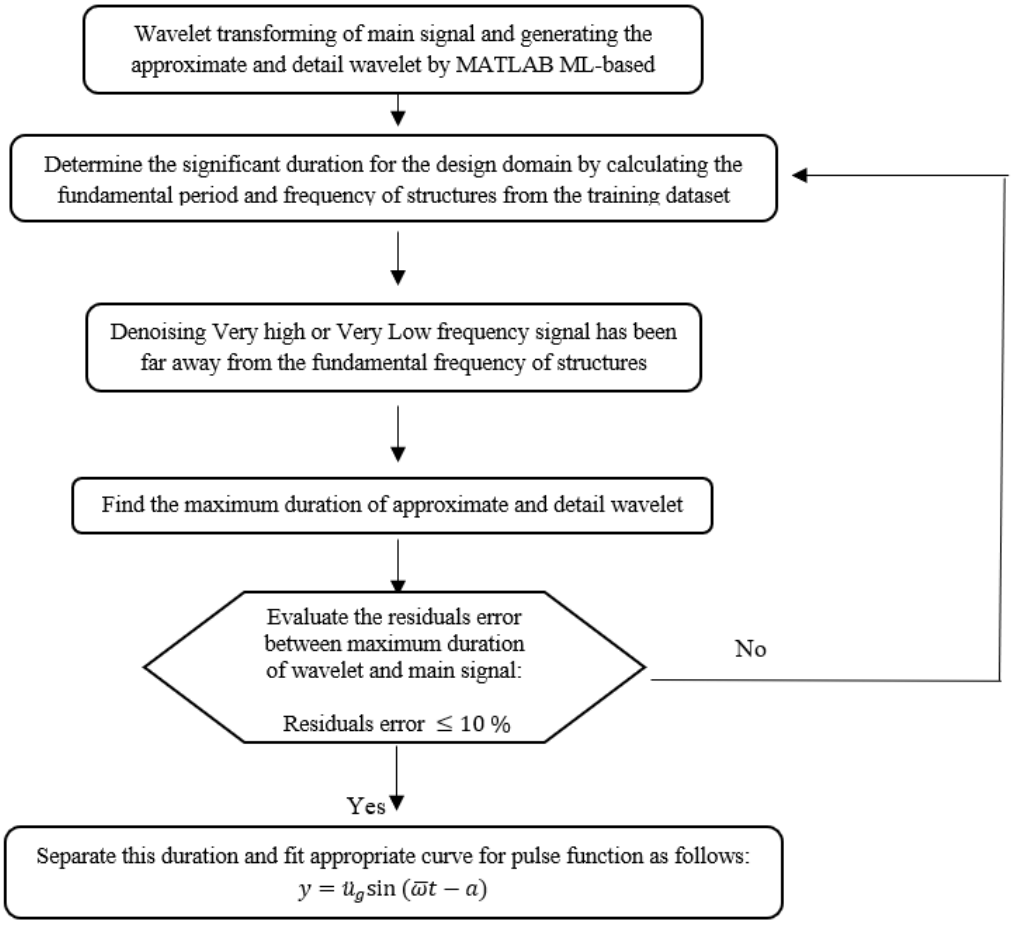

Fig. 6. Flowchart of equivalent pulse generation by WTMLM.

This decomposition is iterated until the transformed signal's characteristics converge with those of the selected base wavelet, namely the Meyer wavelet [29], chosen for its similarity to real seismic signals (Fig. 5b). The final transform is obtained by filtering out frequency content outside the structure's design frequency range. Fig. 6 presents the flowchart of the proposed method. As

shown, fitting functions for both the approximate and detail wavelets are derived using the sinusoidal function $y = \ddot{u}_g \sin(\bar{\omega}t - a)$, where $\ddot{u}_g$ is the pulse acceleration amplitude, $\bar{\omega}$ represents the frequency, and a denotes the phase difference.

2.7. Solution of the dynamic equilibrium equation

As previously stated, the data complexity of real earthquake records prevents the development of a theoretical closed-form solution for Eq. 28. To resolve this, the force function on the right-hand side of Eq. 28 is replaced with the proposed equivalent force function as follows:

$$P_{eq}(\mathrm{t}) = -[M]\{I\}(\ddot{u}) = -[M]\{I\}\ddot{u}_g \sin(\bar{\omega}t - a) \tag{32}$$

Here, $\ddot{u}_g \sin(\bar{\omega}t - a)$ is the fitted acceleration function for the main earthquake record, generated using the proposed WTMLM as explained in the previous subsection (see Fig. 6). Finally, by substituting Eqs. 25 through 27 into Eq. 32, the resulting dynamic equilibrium equation is formulated as follows:

$$\begin{bmatrix} \frac{\sum_{i=1}^{n}(m_i \cdot \Delta_{i.SYS})}{\Delta_d} & 0 & 0 \\ 0 & \frac{\gamma_{i-1}h_{i-1} + \gamma_i h_i}{g} & 0 \\ 0 & 0 & \frac{\gamma_{i-1}h_{i-1} + \gamma_i h_i}{g} \end{bmatrix} \begin{Bmatrix} \ddot{u}_{st} \\ \ddot{u}_{s1} \\ \ddot{u}_{s2} \end{Bmatrix} + \begin{bmatrix} 2 \cdot \xi_{eq.RC} \cdot (\frac{2\pi}{T_e})^2 & -2 \cdot \xi_{eq.RC} \cdot (\frac{2\pi}{T_e})^2 & 0 \\ -2 \cdot \xi_{eq.RC} \cdot (\frac{2\pi}{T_e})^2 & C_{s1} + 2 \cdot \xi_{eq.RC} \cdot (\frac{2\pi}{T_e})^2 & -C_{s1} \\ 0 & -C_{s1} & C_{s1} + C_{s2} \end{bmatrix} \begin{Bmatrix} \dot{u}_{st} \\ \dot{u}_{s1} \\ \dot{u}_{s2} \end{Bmatrix}$$
$$+ \begin{bmatrix} K_e & -K_e & 0 \\ -K_e & \frac{G_{s1}}{2h_{s1}} + K_e & -\frac{G_{s1}}{2h_{s1}} \\ 0 & -\frac{G_{s1}}{2h_{s1}} & \frac{G_{s1}}{2h_{s1}} + \frac{G_{s2}}{2h_{s2}} \end{bmatrix} \begin{Bmatrix} u_{st} \\ u_{s1} \\ u_{s2} \end{Bmatrix} \tag{33}$$
$$= -\begin{bmatrix} \frac{\sum_{i=1}^{n}(m_i \cdot \Delta_{i.SYS})}{\Delta_d} & 0 & 0 \\ 0 & \frac{\gamma_{i-1}h_{i-1} + \gamma_i h_i}{g} & 0 \\ 0 & 0 & \frac{\gamma_{i-1}h_{i-1} + \gamma_i h_i}{g} \end{bmatrix} \{\mathrm{I}\}\ddot{u}_g \sin(\bar{\omega}t - a)$$

The dynamic equilibrium equation is solved using the characteristic equation method. This approach is valid because the equivalent stiffness, as defined by Eqs. 1 and 9, is treated as a linear parameter. This linearization permits the correct application of modal analysis. The eigenvalues obtained from solving the characteristic equation yield the system's natural frequencies, ω_n, which are then assembled into the modal matrix $[\phi]$ as follows:

$$\left| \begin{bmatrix} K_e & -K_e & 0 \\ -K_e & \frac{G_{s1}}{2h_{s1}} + K_e & -\frac{G_{s1}}{2h_{s1}} \\ 0 & -\frac{G_{s1}}{2h_{s1}} & \frac{G_{s1}}{2h_{s1}} + \frac{G_{s2}}{2h_{s2}} \end{bmatrix} - \omega_n{}^2 \begin{bmatrix} \frac{\sum_{i=1}^{n}(m_i \cdot \Delta_{i.SYS})}{\Delta_d} & 0 & 0 \\ 0 & \frac{\gamma_{i-1}h_{i-1} + \gamma_i h_i}{g} & 0 \\ 0 & 0 & \frac{\gamma_{i-1}h_{i-1} + \gamma_i h_i}{g} \end{bmatrix} \right| = 0 \tag{34}$$

$$[\omega_n] = \begin{bmatrix} \omega_1 \\ \omega_2 \\ \omega_3 \end{bmatrix} \tag{35}$$

By using the obtained natural frequencies, the modal matrix could be calculated as follows:

$$[\phi_n] = \begin{bmatrix} \phi_{11} & \phi_{12} & \phi_{13} \\ \phi_{21} & \phi_{22} & \phi_{23} \\ \phi_{31} & \phi_{32} & \phi_{33} \end{bmatrix} \tag{36}$$

The displacement vector {u} is expressed in terms of its modal contributions as follows:

$$u(t) = \sum_{n=1}^{N} \phi_{\mathrm{n}} y_n(t) \tag{37}$$

Substituting Eq. 37 in Eq. 24 gives:

$$\sum_{n=1}^{N} m\phi_{\mathrm{n}} \ddot{y}_n(t) + \sum_{n=1}^{N} c\phi_{\mathrm{n}} \dot{y}_n(t) + \sum_{n=1}^{N} k\phi_{\mathrm{n}} y_n(t) = P(t) \tag{38}$$

By multiplying ϕ_n^T, the uncoupled form of Eq. 38 can be rewritten as follows [8]:

$$\sum_{n=1}^{N} \phi_n^T m \phi_n \ddot{y}_n(t) + \sum_{n=1}^{N} \phi_n^T c \phi_n \dot{y}_n(t) + \sum_{n=1}^{N} \phi_n^T k \phi_n y_n(t) = \phi_n^T P(t) \quad (39)$$

According to orthogonality relations, the Eq. 39 can be formed as Eq. 40.

$$M_n \ddot{y}_n(t) + C_n \dot{y}_n(t) + K_n y_n(t) = P_n(t) \quad (40)$$

Where $M_n = \phi_n^T m \phi_n$, $C_n = \phi_n^T c \phi_n$, $K_n = \phi_n^T k \phi_n$ and $P_n(t) = \phi_n^T P(t)$

Analogous to a SDOF system under a harmonic force $P_n(t)$, the steady-state solution for each modal degree of freedom n is given by:

$$y_n(t) = \frac{P_{nt}}{K_n} \cdot \frac{1}{\sqrt{\left(1 - (\bar{\omega}/\omega_n)^2\right)^2 + \left(2\xi_n(\bar{\omega}/\omega_n)\right)^2}} \quad (41)$$

Considering the proposed equivalent force function of Eq. 32 and Eq. 40, the P_{nt} is defined as follows:

$$P_{nt} = \phi_n^T P(t) = \phi_n^T \begin{Bmatrix} m_e \\ m_{s1} \\ m_{s2} \end{Bmatrix} \ddot{u}_g \sin(\bar{\omega} t - a) \quad (42)$$

Also, $K_n = \phi_n^T k \phi_n$ for each degree of freedom n. Since $-1 \leq \sin(x) \leq 1$, The maximum final response of the system is calculated as follows:

$$y_{max.n} = \frac{\phi_n^T \left(\frac{\sum_{i=1}^{n}(m_i \cdot \Delta_{i.SYS})}{\Delta_d} + \frac{\gamma_{i-1}h_{i-1} + \gamma_i h_i}{g} + \frac{\gamma_{i-1}h_{i-1} + \gamma_i h_i}{g}\right) \cdot \ddot{u}_g / K_n}{\sqrt{\left(1 - (\bar{\omega}/\omega_n)^2\right)^2 + \left(2\xi_n(\bar{\omega}/\omega_n)\right)^2}} \quad (43)$$

The equivalent system of this study has three DOFs, including structural component, soil layer 1, and 2, as shown in Fig. 4. The solutions of each DOF are called y_{st}, y_{s1}, and y_{s2} obtained by Eq. 44.

$$y_{st} = \frac{\left(\frac{\sum_{i=1}^{n}(m_i \cdot \Delta_{i.SYS})}{\Delta_d}\phi_{11} + \frac{\gamma_1 h_1}{g}\phi_{21} + \frac{\gamma_1 h_1 + \gamma_2 h_2}{g}\phi_{31}\right) \cdot \ddot{u}_g / K_1}{\sqrt{\left(1 - (\bar{\omega}/\omega_1)^2\right)^2 + \left(2\xi_n(\bar{\omega}/\omega_1)\right)^2}}$$

$$y_{s1} = \frac{\left(\frac{\sum_{i=1}^{n}(m_i \cdot \Delta_{i.SYS})}{\Delta_d}\phi_{12} + \frac{\gamma_1 h_1}{g}\phi_{22} + \frac{\gamma_1 h_1 + \gamma_2 h_2}{g}\phi_{32}\right) \cdot \ddot{u}_g / K_2}{\sqrt{\left(1 - (\bar{\omega}/\omega_2)^2\right)^2 + \left(2\xi_n(\bar{\omega}/\omega_2)\right)^2}} \quad (44)$$

$$y_{s2} = \frac{\left(\frac{\sum_{i=1}^{n}(m_i \cdot \Delta_{i.SYS})}{\Delta_d}\phi_{13} + \frac{\gamma_1 h_1}{g}\phi_{23} + \frac{\gamma_1 h_1 + \gamma_2 h_2}{g}\phi_{33}\right) \cdot \ddot{u}_g / K_3}{\sqrt{\left(1 - (\bar{\omega}/\omega_3)^2\right)^2 + \left(2\xi_n(\bar{\omega}/\omega_3)\right)^2}}$$

Where, the h_1 and h_2 are the half thickness of soil layers 1 and 2, respectively. Using Eqs. 37 and 44, the displacements of each DOF are calculated as Eq. 45. Furthermore, the Square-Root-of-Sum-of-Squares (SRSS) method has been used to obtain the maximum responses.

$$\begin{Bmatrix} u_{st} = \sqrt{(\varphi_{11}y_{st})^2 + (\varphi_{12}y_{s1})^2 + (\varphi_{13}y_{s2})^2} \\ u_{s1} = \sqrt{(\varphi_{21}y_{st})^2 + (\varphi_{22}y_{s1})^2 + (\varphi_{23}y_{s2})^2} \\ u_{s2} = \sqrt{(\varphi_{31}y_{st})^2 + (\varphi_{32}y_{s1})^2 + (\varphi_{33}y_{s2})^2} \end{Bmatrix} \quad (45)$$

Hence, the drift ratio of the structure with the SSI effect is calculated.

$$\theta_{st-SSI} = \frac{u_{st} - u_{s1}}{h_e} \quad (46)$$

The modified demand displacement with the SSI effect is also obtained.

$$\Delta_{st-SSI} = \theta_{st-SSI} \cdot h_e \quad (47)$$

The modified period is then derived from the modified displacement response spectrum using Eq. 47. Subsequently, the modified stiffness and base shear of the structure, accounting for SSI effects, are calculated as follows:

$$K_{e.st-SSI} = \frac{4\pi^2 m_e}{T_{e.st-SSI}^2} \quad (48)$$

$$V_{st-SSI} = \Delta_{st-SSI} \cdot K_{e.st-SSI} \quad (49)$$

Finally, the modified base shear, which accounts for SSI effects, is distributed over the height of the structure to determine the lateral force at each story level i as follows:

$$F_{i.total} = \frac{m_i \Delta_i}{\sum_{i=1}^{n} m_i \Delta_i} V_{st-SSI} \tag{50}$$

3. Summary of proposed method

The design process for the proposed Wavelet Transform-based Machine Learning Method (WTMLM) for RC frames with SSI effects is summarized in the flowchart in Fig. 7, which is based on the equations developed in the preceding sections. Given that the equivalent stiffness depends on the components of the stiffness matrix, the design procedure is iterative. As illustrated in Fig. 7, the procedure begins by defining the target performance level, geometric parameters, and material properties of the soil and structure. Subsequently, the characteristics of the equivalent SDOF system and the effective structural stiffness are calculated. The seismic input is then transformed into an equivalent pulse function using the proposed WTMLM for use as the force function on the right-hand side of the dynamic equilibrium equation. Next, the dynamic equilibrium equation for the structure with SSI effects is formulated using the mass, stiffness, and damping matrices. This equation is solved to obtain the final displacement response, from which the modified demand displacement incorporating SSI effects is determined. The effective period of the system is then derived using this modified displacement. The resulting modified structural stiffness is calculated and compared with the effective stiffness from the initial step. The equivalent stiffness is updated iteratively until convergence is achieved between successive stiffness values. Upon convergence, the final design base shear is computed. This base shear is then distributed over the height of the structure, enabling the final frame design according to the ACI 318 code [30]. Furthermore, the procedural steps of the proposed WTMLM are detailed in Fig. 8.

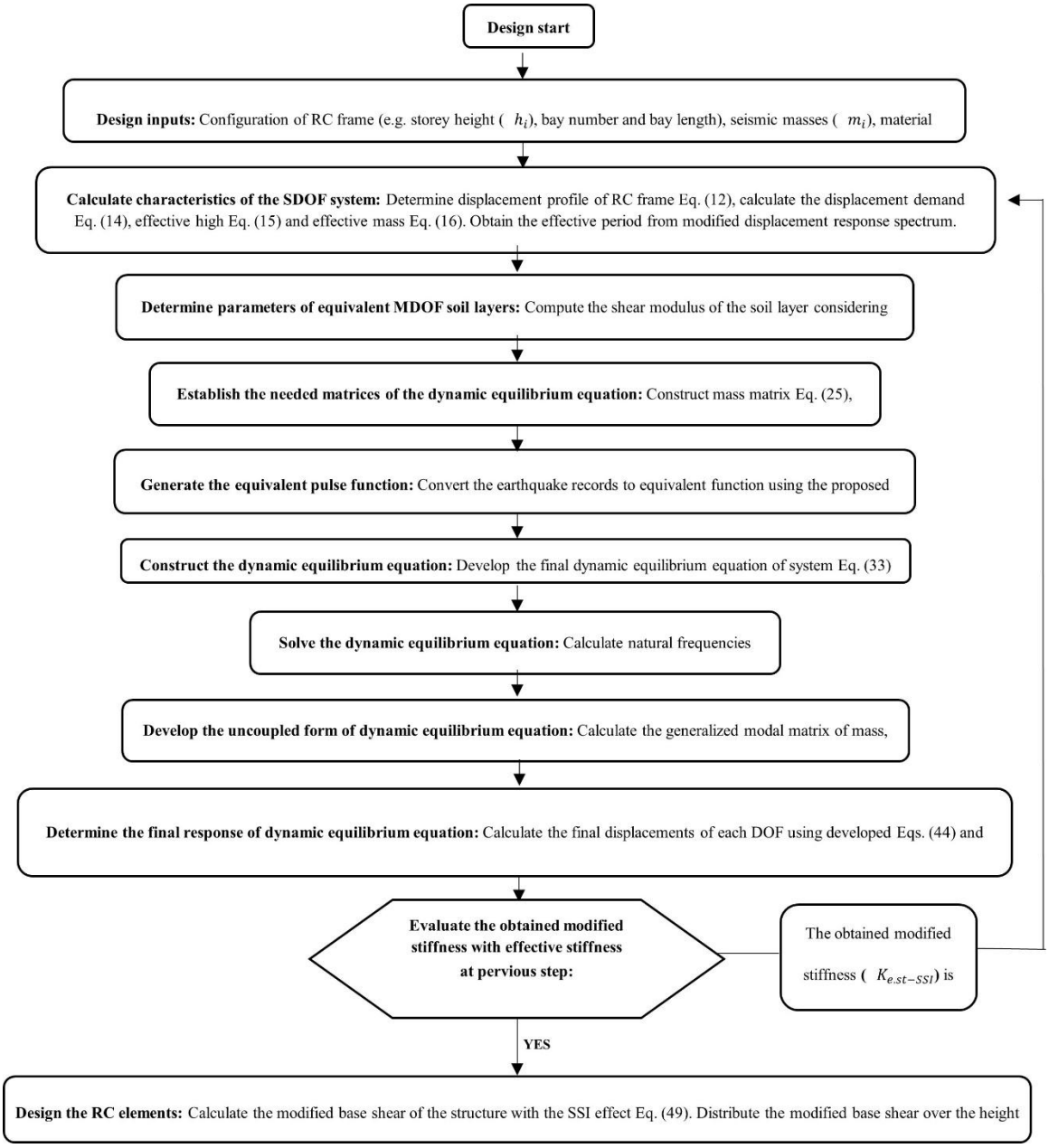

Fig. 7. Flowchart of proposed wavelet transform-based machine learning method (WTMLM).

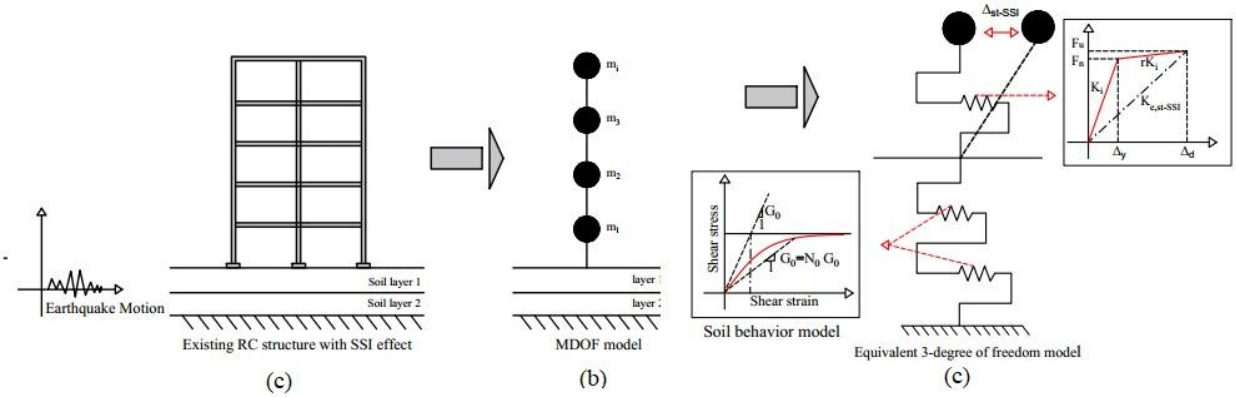

Fig. 8. Framework of WTMLM: (a) Existing RC frame with two layers of soil (b) MDOF model (c) Proposed equivalent three-degree-of-freedom model.

4. Application of the proposed WTMLM to case study, models

4.1. Seismic ground motion inputs

A set of seven real ground motions was selected from the PEER NGA-West2 database to design the case study structures, as listed in Table 2. Fig. 9 shows that the spectral accelerations of these records were scaled to match the design spectrum for site class B, as specified in ASCE/SEI 7-22 [1]. Amplitude scaling was adopted in accordance with ASCE 7-22 [1], with each record scaled individually so that its 5% damped response spectrum, averaged over the period range from 0.2T to 1.5T, does not fall below the corresponding design spectrum. For the 3- storey case study frames, this period range spans approximately 0.076 s to 0.574 s, as shown in Fig. 9. No spectral matching was employed, ensuring the preservation of the original frequency content and non-stationary characteristics of the ground motions. Following the procedure in the flowchart of Fig. 6, the seven earthquake records were converted into seven pairs of approximate and detail functions. For instance, Figs. 10 and 11 display the approximate and detail wavelets for the R4 and R6 signals alongside their equivalent pulse functions. The equivalent pulses generated with WTMLM for the remaining signals are provided in Table 3. It should be noted that all generated pulse signals are used in the following subsection to formulate the dynamic equilibrium equations for the case study structures, including SSI effects.

Table 2. Details of earthquake signals.

No.	Earthquake name	Station	PGA (m/s^2)
R1	Cape Mendocino, 1992	89324 Rio Dell Overpass-FF	0.385
R2	Chi-Chi, Taiwan, 1999	TCU045	0.474
R3	Kocaeli, Turkey, 1999	Arcelik	0.149
R4	Landers, 1992	23 Coolwater	0.283
R5	Loma Prieta, 1989	1652 Anderson Dam	0.240
R6	Northridge, 1994	24688 LA –UCL Grounds	0.278
R7	San Fernando, 1971	128 Lake Hughes	0.283

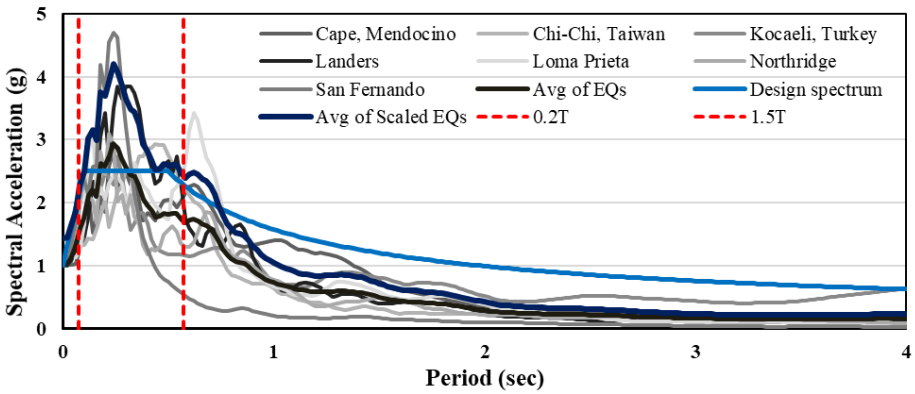

Fig. 9. Response spectra of the scaled records and the design spectrum for 3-storey structure.

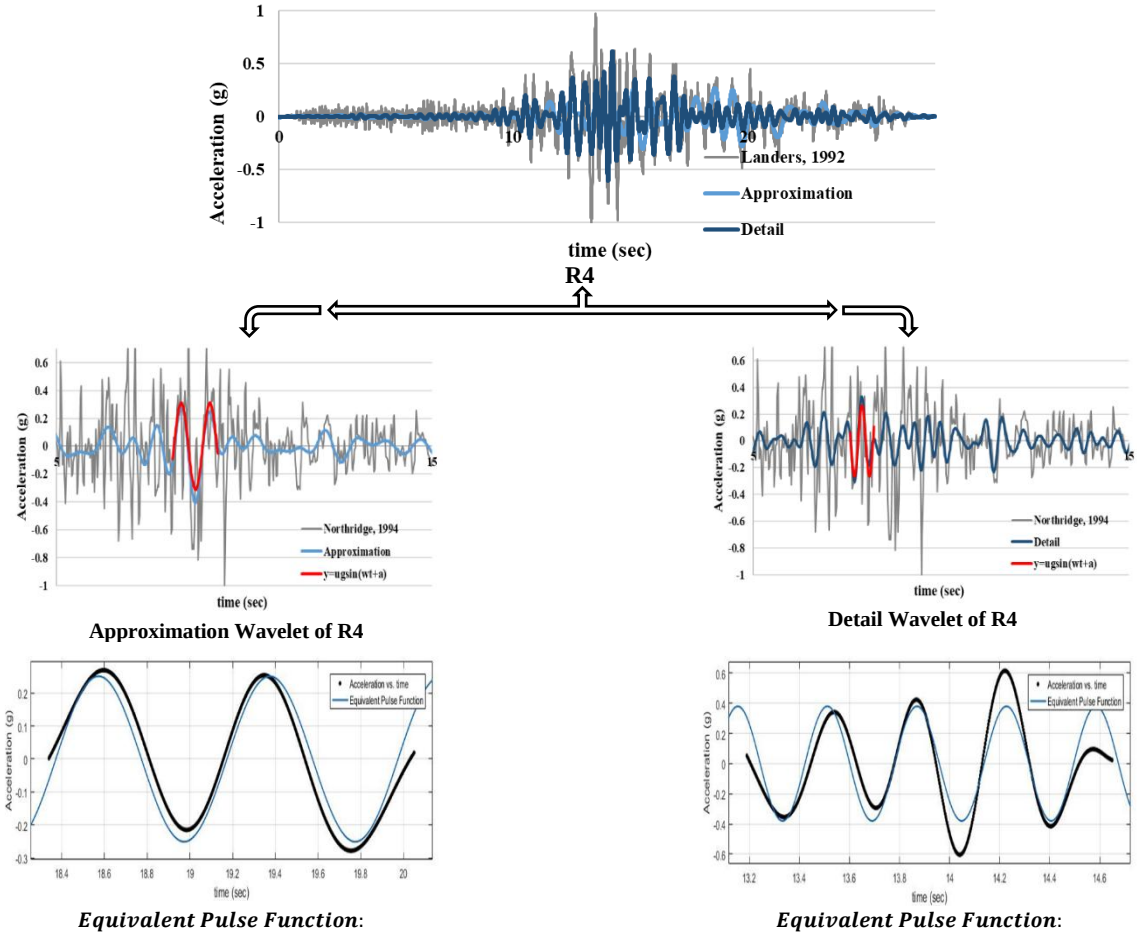

Fig. 10.WTMLM flowchart for equivalent pulse signal generation (example: record R4).

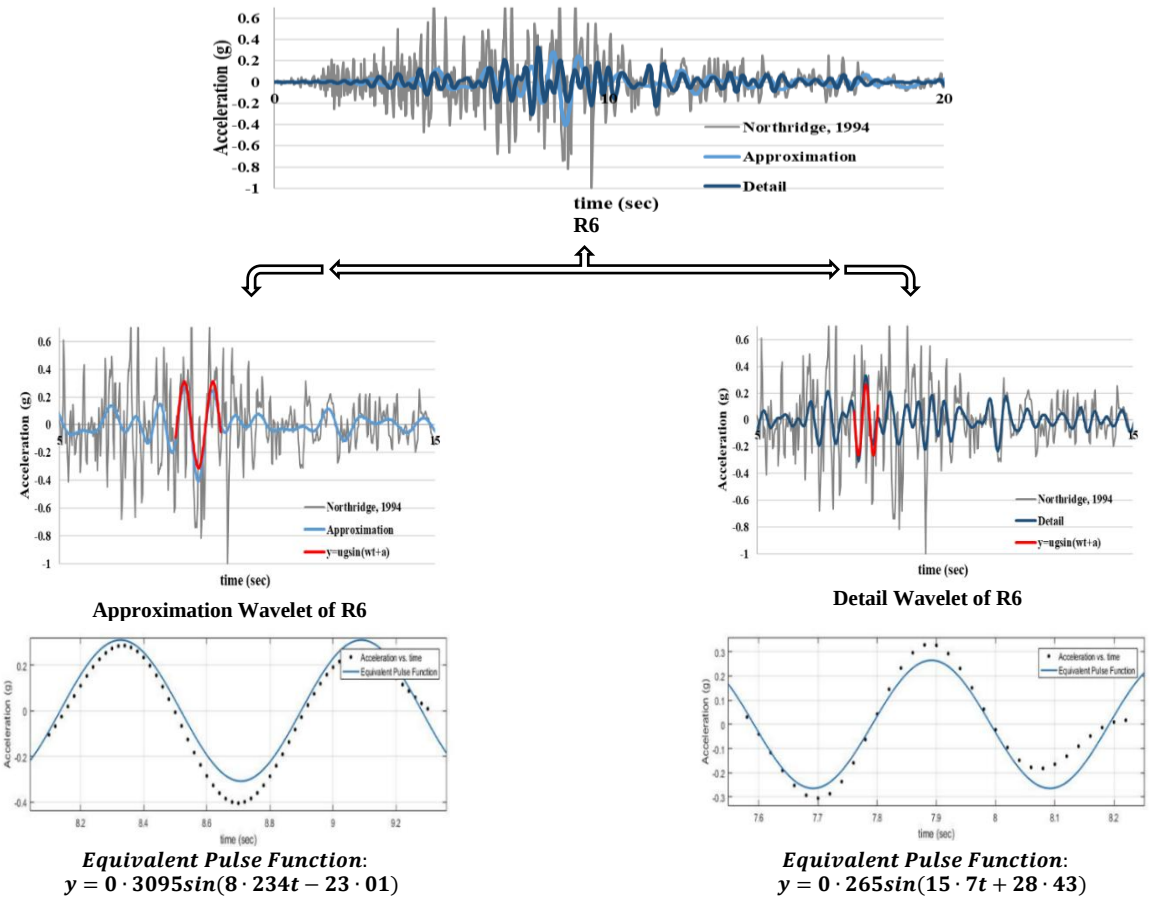

Fig. 11. WTMLM flowchart for equivalent pulse signal generation (example: record R6).

Table 3. Characteristics of equivalent pulse function.

Signal Names	Equivalent Pulse Function From Approximation Wavelet	Equivalent Pulse Function From Detail Wavelet
R1	$y = 0 \cdot 189sin(4 \cdot 21t + 0 \cdot 47)$	$y = 0 \cdot 3941sin(7 \cdot 98t - 14 \cdot 41)$
R2	$y = 0 \cdot 1541sin(4 \cdot 44t + 84 \cdot 05)$	$y = 0 \cdot 6713sin(13 \cdot 12t - 5 \cdot 90)$
R3	$y = 0 \cdot 2991sin(1 \cdot 67t + 0 \cdot 86)$	$y = 0 \cdot 3041sin(16 \cdot 03t - 79 \cdot 06)$
R4	$y = 0 \cdot 2511sin(7 \cdot 84t - 12 \cdot 17)$	$y = 0 \cdot 38sin(17 \cdot 56t - 3 \cdot 23)$
R5	$y = 0 \cdot 4159sin(9 \cdot 21t - 24 \cdot 51)$	$y = 0 \cdot 4414sin(13 \cdot 81t - 15 \cdot 82)$
R6	$y = 0 \cdot 3095sin(8 \cdot 23t - 23 \cdot 01)$	$y = 0 \cdot 265sin(15 \cdot 70t + 28 \cdot 43)$
R7	$y = 0 \cdot 1322sin(13 \cdot 88t - 7 \cdot 51)$	$y = 0 \cdot 8154sin(25 \cdot 80t - 3 \cdot 30)$

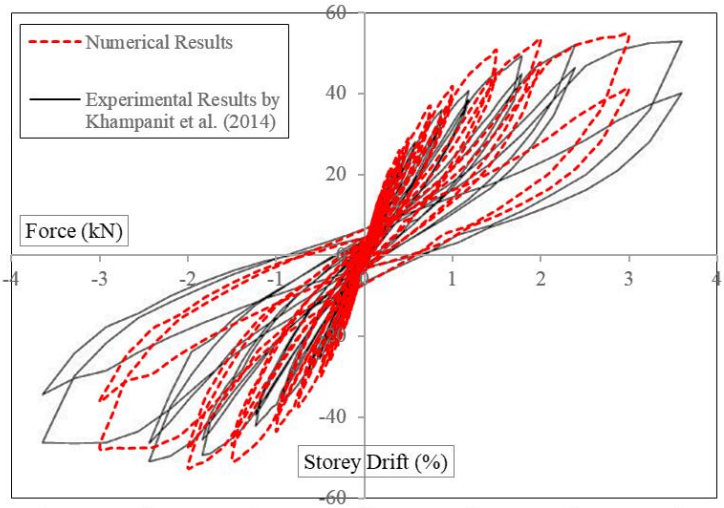

Fig. 12. Comparison of load-displacement responses from the numerical model and the experimental test by Khampanit et al. [31].

4.2. Validation of RC frame numerical modeling

To validate the modeling approach, the numerical model of the RC frame was verified against an experimental test. This study utilizes OpenSees, an open-source software, to perform all numerical analyses. The experimental benchmark is based on the work of Khampanit et al. [31]. Further details on the specifications and dimensions of the experimental RC frame model sections tested under cyclic loading can be found in Khampanit et al. [31]. For the numerical modeling, unconfined and confined concrete were modeled using the *Concrete01* material model, while reinforcing steel was modeled with *Steel02*. The effects of concrete confinement were considered by modeling closed stirrups at specified intervals and defining a separate concrete cover region. The fiber section method was employed to model the beam-column elements. A comparison of the load-displacement responses from the numerical and experimental analyses is presented in Fig. 12. The close agreement between the two results confirms the accuracy of the numerical modeling technique.

4.3. Design of case study structures

Five RC frame structures on two-layer soil profiles were designed using the WTMLM, as illustrated in Fig. 13. As shown in Fig. 14, the structures have a regular plan with moment-resisting connections. The frames are 3, 6, 9, 12, and 15 stories tall, respectively, with a story height of 3.2 m and a two-bay length of 5 m per bay. Uniform dead and live loads of 5 kN/m² and 2 kN/m², respectively, were applied to all floors. The seismic weight for each story was calculated based on the tributary area of the gravity columns. The structural models are founded on two distinct soil layers, whose properties are detailed in Table 4.

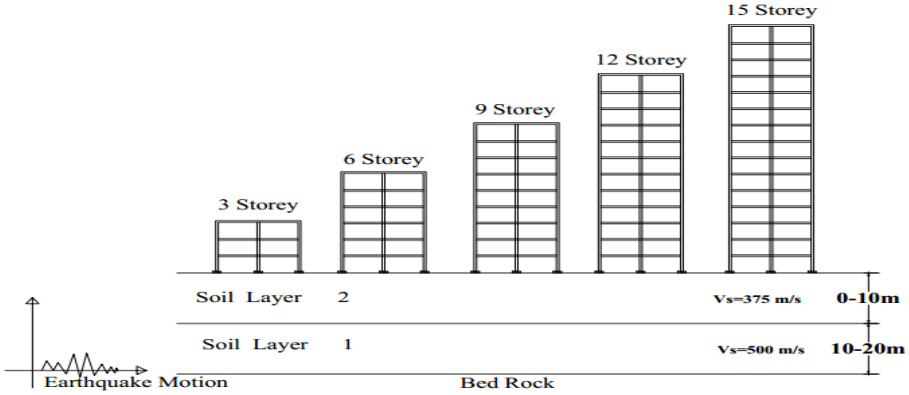

Fig. 13. Structural models of 3, 6, 9, 12 and 15 stories with two soil layers.

The target performance level was set at a 2% drift ratio, corresponding to a repairable damage state [7]. According to Table 4, the shear wave velocities at the bedrock for the first and second soil layers are 375 m/s and 500 m/s, respectively. For each case study, the dynamic equilibrium equation was formulated and solved following the WTMLM outlined in Fig. 6. This analysis was repeated for each ground motion record, and the maximum responses were used to compute the final design base shear. The characteristics of the proposed equivalent three-degree-of-freedom (3DOF) system, including demand displacement, equivalent mass, and effective height, are summarized in Table 5.

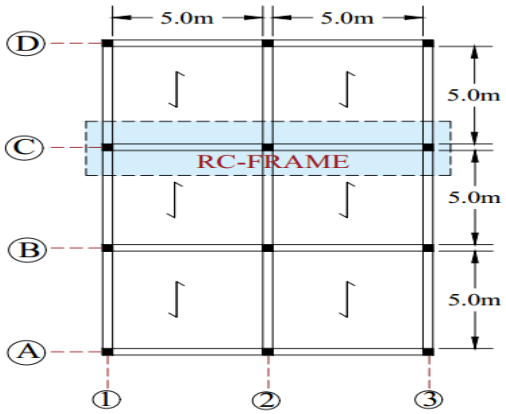

Fig. 14. Plan of Structures.

Table 4. Characteristics of soil layers.

Layer	height (m)	V_s (m/s)	Damping (%)	γ (t/m^3)	G_0 (ton/m^2)	G (ton/m^2)	K_i (ton/m)	m_i (ton)
1	0-10	375	5	1.6	22936	9633	963.3	0.815
2	10-20	500	5	2	50968	21407	2140.7	1.83

Table 5. Design results of WTMLM.

Story	Δ_{d-SSI} (m)	m_e (T)	H_e (m)	μ	T_{e-SSI} (s)	V_{st-SSI} (kN)
3	0.0148	201.84	7.28	1.60	0.333	1063.8
6	0.0062	381.61	13.50	1.51	0.213	2059.1
9	0.0133	559.53	19.74	1.45	0.309	3074.2
12	0.0327	736.94	25.98	1.40	0.481	4123.3
15	0.0502	914.15	32.21	1.35	0.641	4420.4

Table 6. Final results of lateral loads.

Level	Lateral Forces of WTMLM (kN)				
	3-storey frame	6-storey frame	9-storey frame	12-storey frame	15-storey frame
1	201.75	114.67	80.59	62.64	43.75
2	366.82	219.37	156.58	122.60	86.03
3	495.20	314.09	227.96	179.91	126.82
4		398.85	294.74	234.55	166.14
5		473.63	356.92	286.52	203.96
6		538.45	414.48	335.83	240.30
7			467.44	382.47	275.16
8			515.80	426.45	220.36
9			559.55	467.77	308.53
10				506.42	370.83
11				542.40	399.76
12				575.72	427.20
13					453.16
14					477.63
15					500.62

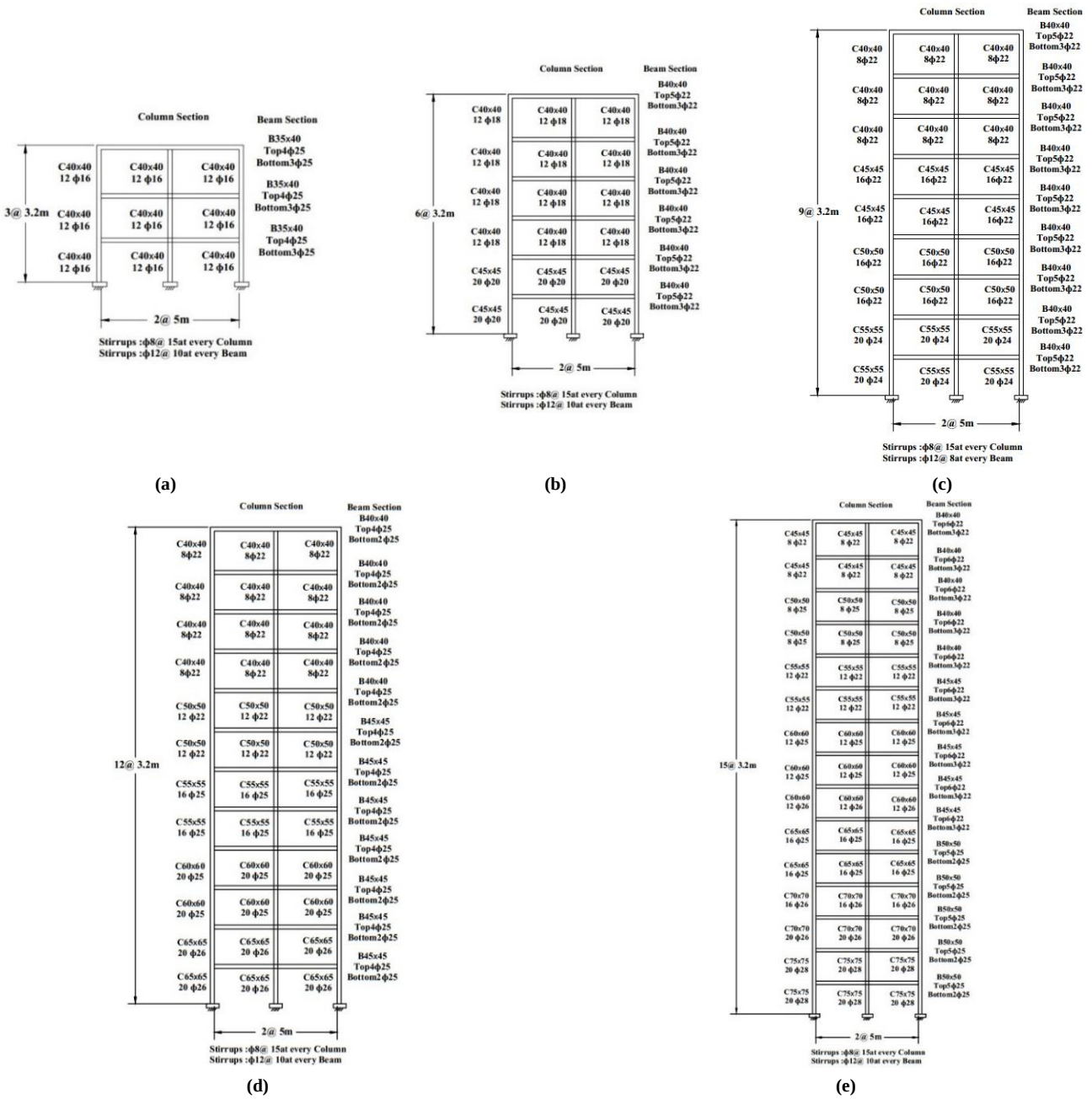

Fig. 15. Final design section results: a) 3-storey, b) 6-storey, c) 9-storey, d) 12-storey, e) 15-storey.

The final design base shear, calculated using Eq. 49, is presented in the last column of Table 5. Table 6 shows the resulting lateral forces distributed over the height of each frame. These forces are used to determine the design forces and moments for the structural members. All members are designed based on structural analysis, following the strong column-weak beam principle to ensure plastic hinges form at the beam ends [30]. The final cross-sections of the designed RC frames are shown in Fig. 15.

5. Nonlinear time-history analysis (NTHA) results

To validate the proposed WTMLM, all designed frames are evaluated using nonlinear time-history analysis (NTHA) with real earthquake records. The NTHA employs a two-dimensional model constrained against out-of-plane deformation. All analyses are performed using the open-source software OpenSees. The Concrete01 and Steel02 material models are used for concrete and reinforcing steel, respectively. Concrete confinement is modeled by specifying closed stirrups at appropriate intervals and defining a separate concrete cover. Beam-column sections are modeled using the fiber method. Gravity loads are applied as distributed loads on the beams using the eleLoad command, while seismic masses are assigned to nodes using the mass command. Geometric nonlinearity and P-Delta effects are incorporated using the geomTransf PDelta command for column elements. All NTHAs are performed using the Newmark integration method with $\gamma = 0.5$ and $\beta = 0.25$. The analysis time step is defined by the original earthquake record. A tangent stiffness-proportional Rayleigh damping model with 5% viscous damping is assigned to the numerical models.

Soil layers are modeled using shear beam theory; each layer is represented by a concentrated mass and springs, as illustrated in Fig. 1. To validate the proposed WTMLM, NTHAs were performed on all five frames using the seven real ground motion records. The inter-story drift ratios and displacement profiles for each frame are presented in the following figures. Figs. 16 to 18 show the

inter-story drift distributions from the analyses. The drift profile indicates that the drift ratio is lowest at the first story, increases to a maximum at approximately mid-height, and then decreases toward the top of the frame. In these profiles, the horizontal axis represents the drift ratio (in percent), and the vertical axis represents the story level. The target performance level is marked by a vertical dashed line at 2% drift, corresponding to the repairable damage state. Fig. 16a presents the inter-story drift ratio diagram for the three-story RC frame designed without SSI effects, while Fig. 16b shows the same diagram including SSI effects. A design capacity line, representing the minimum capacity of structural and non-structural members for the repairable damage level, is also included. As shown in both figures, the average inter-story drift across the seven earthquake records remains below this capacity line. This confirms that the WTMLM accurately achieves the target performance level.

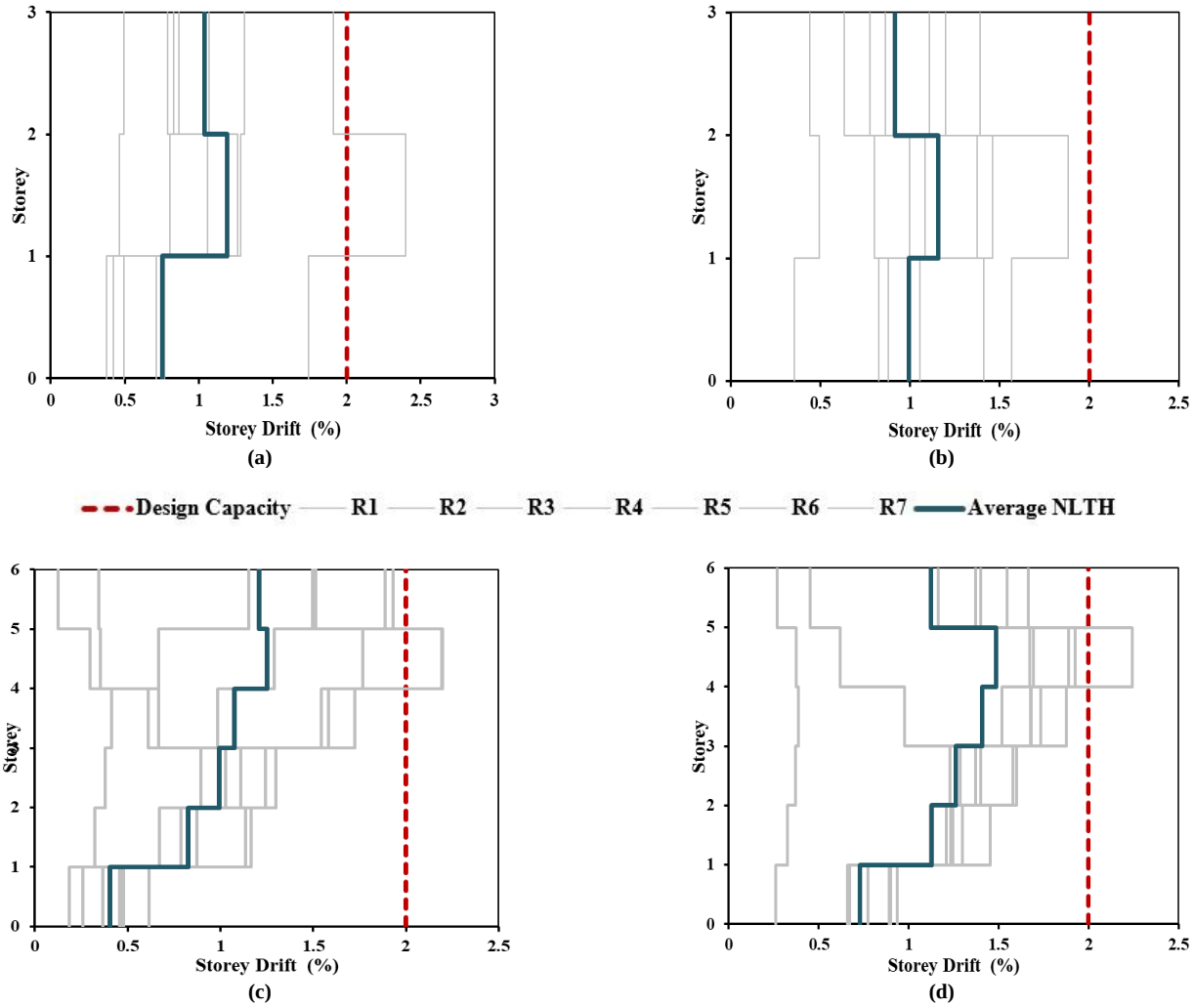

Fig. 16. The interstorey drift profiles obtained by NTHA of frames designed by WTMLM: (a) 3-storey frame without SSI effect, (b) 3-storey frame with SSI effect, (c) 6-storey frame without SSI effect, (d) 6-storey frame with SSI effect.

The results for the 6-story frame are shown in Figs. 16c and 16d, while those for the 9- and 12-story frames are presented in Figs. 17a to 17d. The behavior of these frames is similar to that observed in the 3-story RC frame. However, as shown in Figs. 18a and 18b, the average inter-story drift ratio profile for the 15-story RC frame exceeds the capacity corresponding to the repairable damage performance level, particularly from the 6th to the 10th stories. While this exceeds the repairable limit, the results still satisfy the life safety performance level. The displacement profile was modified according to Eq. 12 to account for higher-mode effects. Nonetheless, the results for the 15-story frame indicate that this modification needs to be intensified for structures of 15 stories or more, likely requiring an increased design base shear. Fig. 19 illustrates the roof displacement time history for all RC frames subjected to the Landers 1992 (R7) earthquake. The plot confirms that the maximum roof displacement in all models is below the acceptable limit, taken as 2% of the structure's height. These results further demonstrate that the proposed WTMLM provides adequate precision in controlling the displacement of the designed structures. It is worth noting that the proposed WTMLM demonstrates accurate prediction of seismic demands and effective capture of ground motion frequency content across multiple RC frame case studies. However, a direct quantitative comparison with existing pulse-based excitation models and SSI replacement oscillator approaches is not included in the present study. This is primarily because no comparable wavelet-based pulse generation methodology currently exists in the literature. Nevertheless, benchmarking against established code-based procedures, evaluating key performance metrics such as displacement error, drift accuracy, and computational efficiency, is essential to further establish the practical advantages of the framework. This critical comparison is identified as a priority for future research.

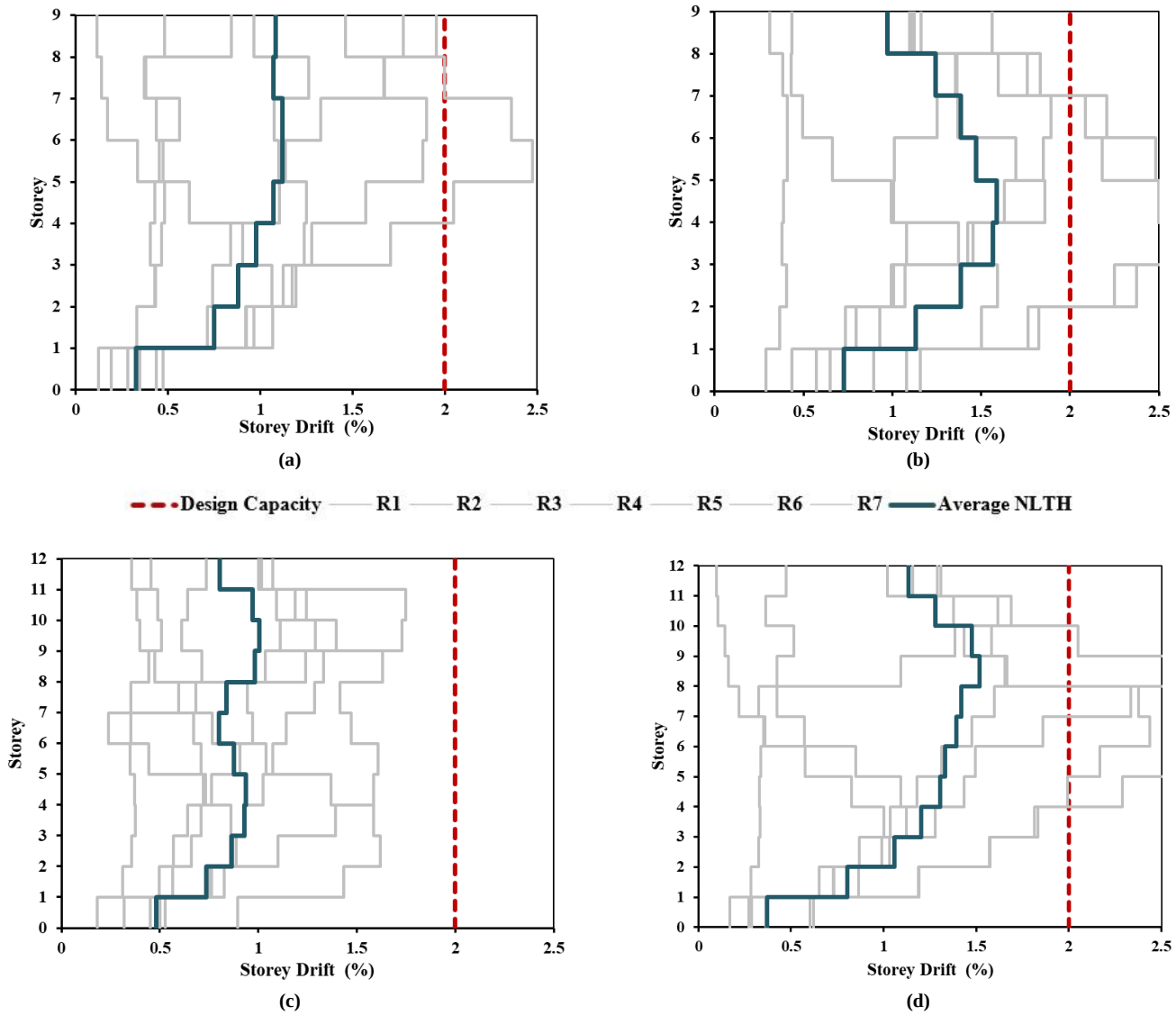

Fig. 17. The interstorey drift profiles obtained by NTHA of frames designed by WTMLM: (a) 9-storey frame without SSI effect, (b) 9-storey frame with SSI effect, (c) 12-storey frame without SSI effect, (d) 12-storey frame with SSI effect.

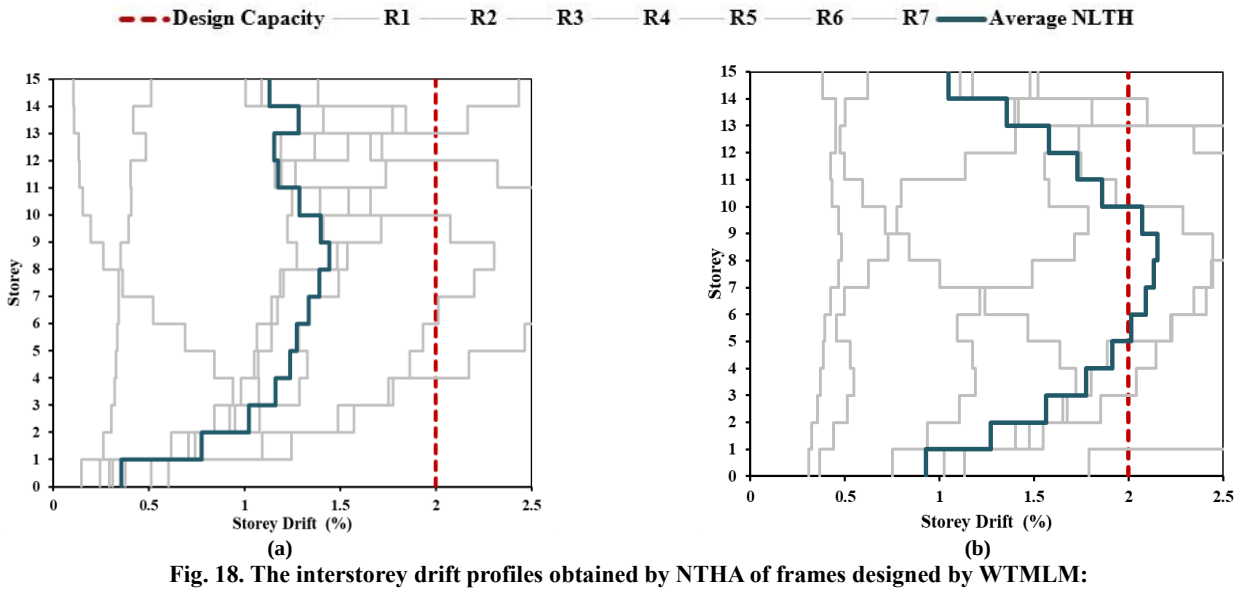

Fig. 18. The interstorey drift profiles obtained by NTHA of frames designed by WTMLM: (a) 15-storey frame without SSI effect, (b) 15-storey frame with SSI effect.

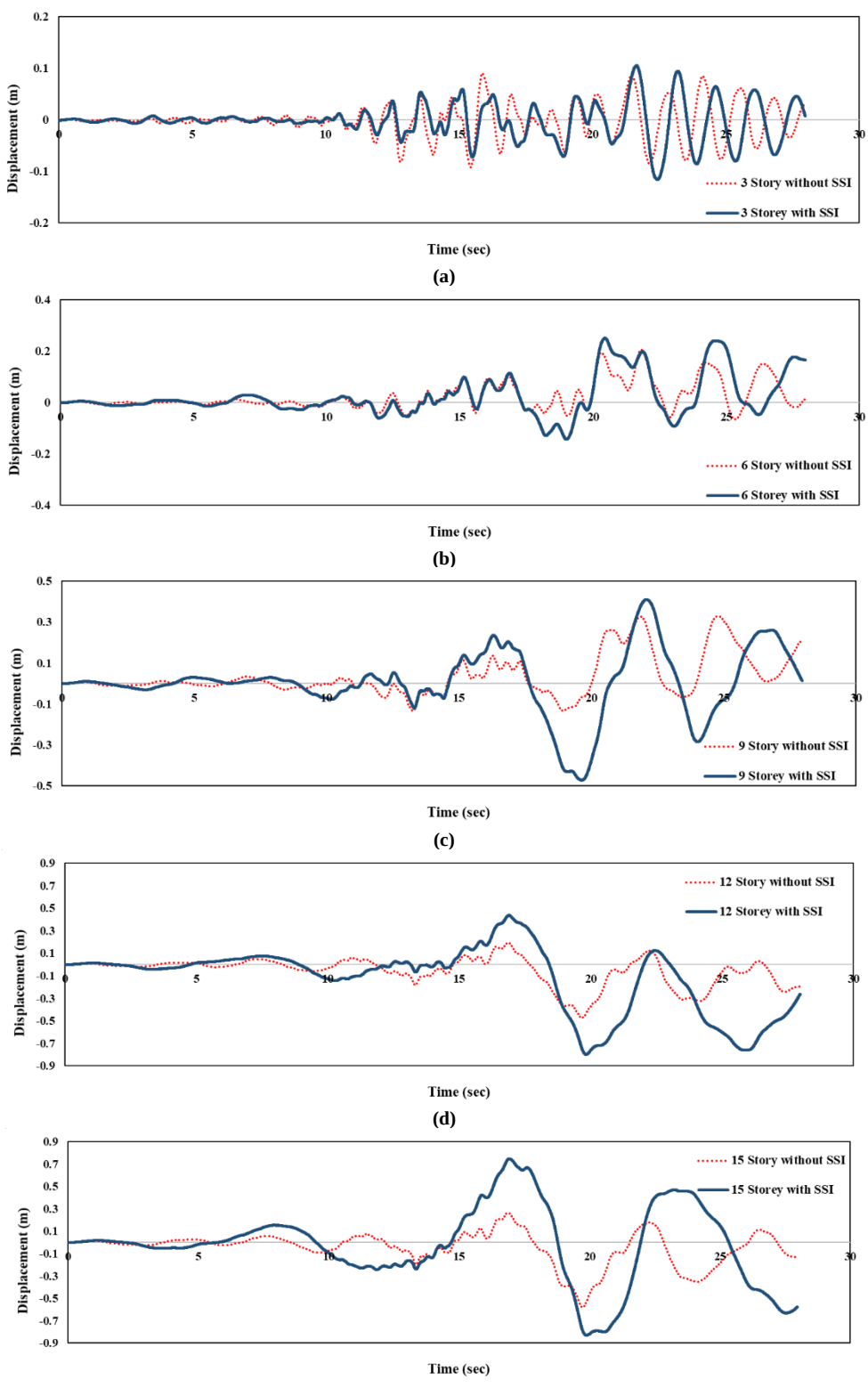

Fig. 19. Comparison of the roof displacement time history of frames designed by WTMLM under the Landers, 1992 (R7) Earthquake with and without the SSI Effect: (a) 3-storey Frame, (b) 6-storey Frame, (c) 9-storey Frame, (d) 12-storey Frame,(e) 15-storey Frame.

The average maximum lateral displacement profiles from the NTHA are presented in Figs. 20 to 24. These figures illustrate the maximum displacement response for each case study structure. For all cases, the average displacement of the RC frames from the NTHA is less than the design capacity displacement. The satisfactory performance of each frame, as evidenced by these results, demonstrates that the proposed WTMLM is a robust method for the seismic design of RC frames incorporating SSI effects. While the proposed WTMLM framework demonstrates promising performance for SSI-inclusive seismic design of RC frames, a systematic comparison with simplified code-based procedures (e.g., ASCE 7 [1] and BHRC-2800 [3]) remains necessary to fully establish its practical advantages. Such a comparative assessment is recommended as a focus of future work. It is noted that prior research by the Farahani et al. [4], has already examined direct displacement-based design incorporating SSI effects using detailed finite element modeling, providing a benchmark for subsequent extensions of the WTMLM framework.

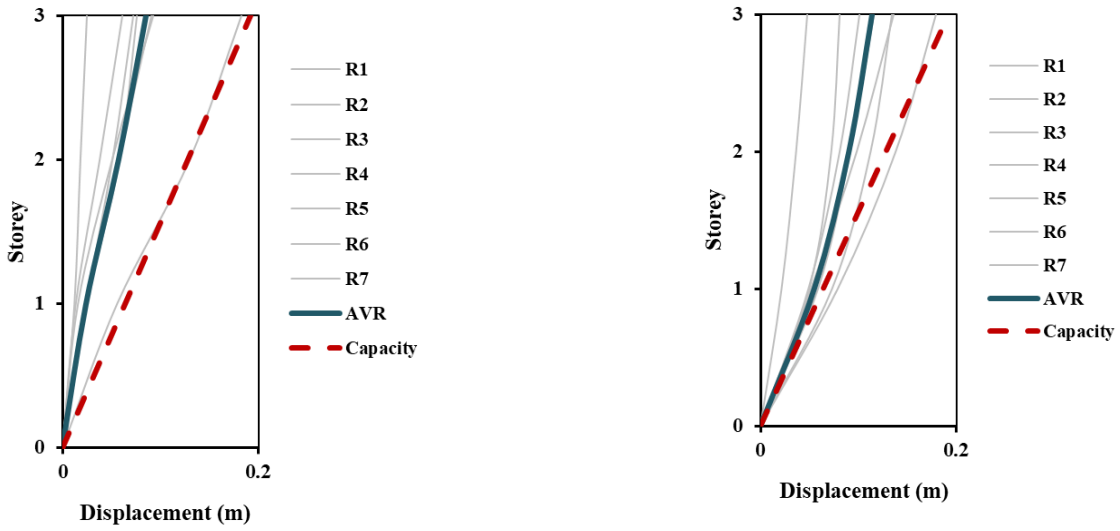

(a) (b)

Fig. 20. The displacement profiles obtained by NTHA of frames designed by WTMLM: (a) 3-storey frame without SSI effect, (b) 3-storey frame with SSI effect.

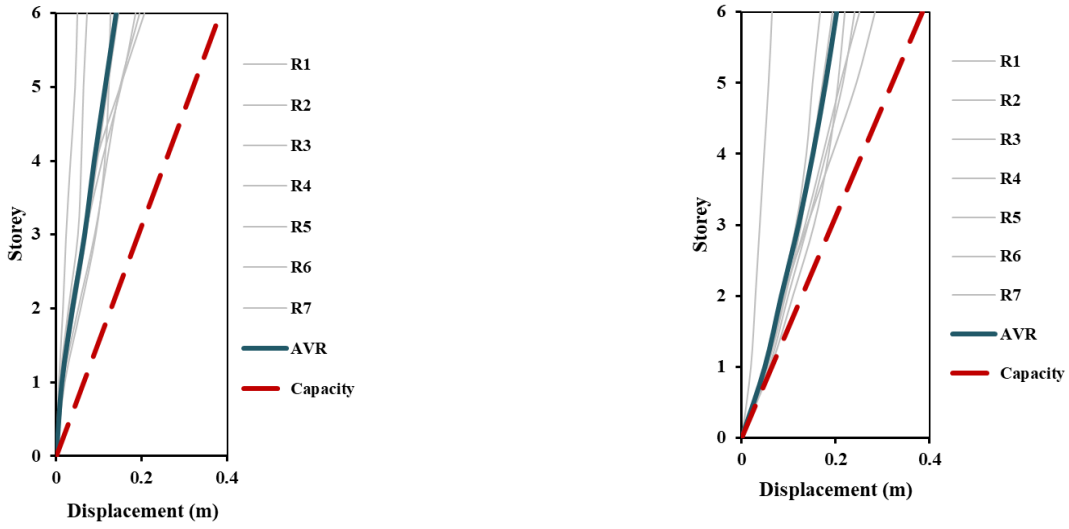

(a) (b)

Fig. 21. The displacement profiles obtained by NTHA of frames designed by WTMLM: (a) 6-storey frame without SSI effect, (b) 6-storey frame with SSI effect.

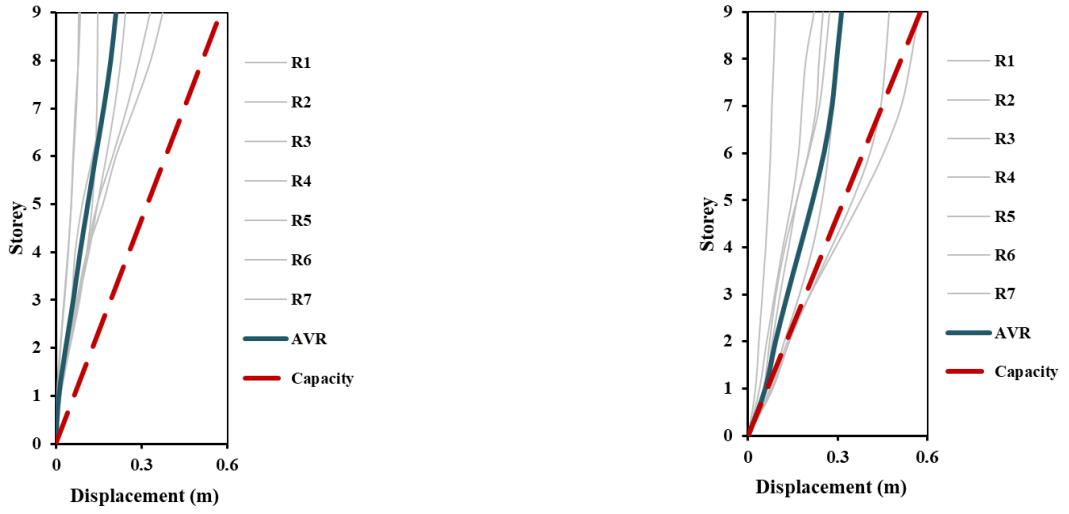

(a) (b)

Fig. 22. The displacement profiles obtained by NTHA of frames designed by WTMLM: (a) 9-storey frame without SSI effect, (b) 9-storey frame with SSI effect.

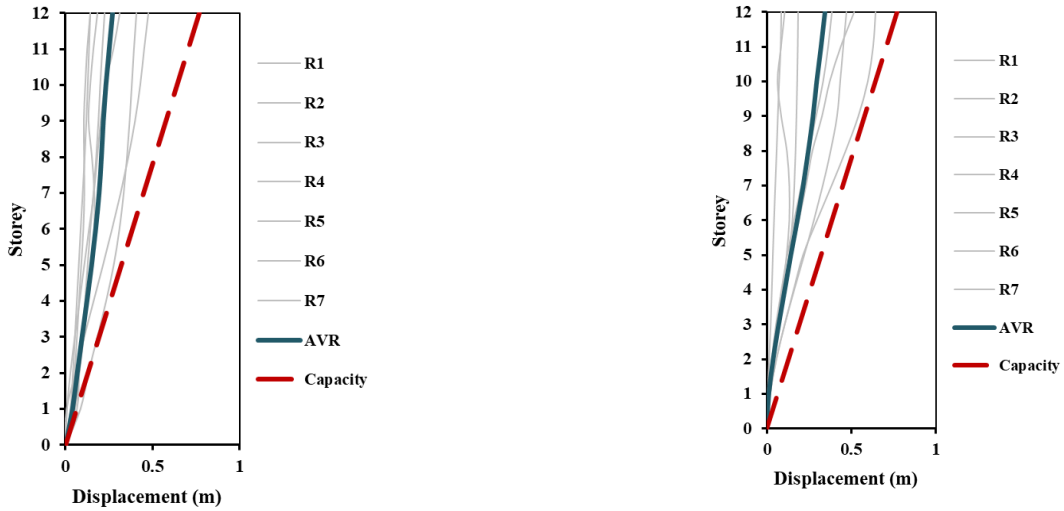

Fig. 23. The displacement profiles obtained by NTHA of frames designed by WTMLM: (a) 12-storey frame without SSI effect, (b) 12-storey frame with SSI effect.

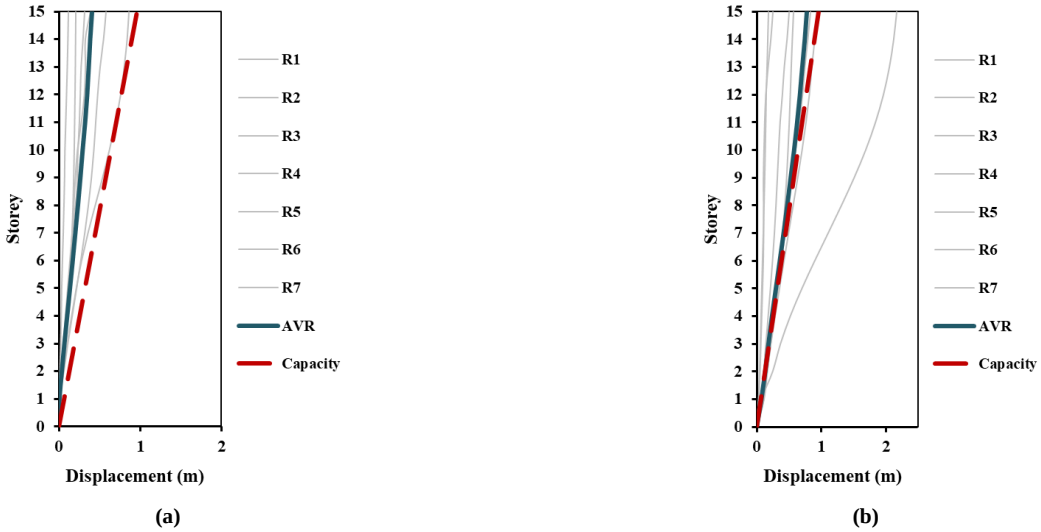

Fig. 24. The displacement profiles obtained by NTHA of frames designed by WTMLM: (a) 15-storey frame without SSI effect, (b) 15-storey frame with SSI effect.

In addition, the WTMLM framework employs equivalent linear soil modeling and linear modal analysis during the design phase to enable efficient pulse generation and system formulation. Seismic performance assessment is conducted exclusively through nonlinear time-history analysis, which fully captures material yielding and geometric nonlinearity of RC frames. The method is applicable to sites where equivalent linear soil representation is valid and for seismic intensities consistent with the employed design spectrum. Extension to strongly nonlinear soil conditions, significant structural yielding, or very high intensity levels requires further refinement and is identified as a priority for future research.

6. An ML-based formula for displacement prediction in RC frame structures

As per Eq. 12, the displacement profile for RC frames proposed by Sullivan et al. [7] is based on a first-mode shape, implying that the inter-story drift ratio decreases with height. This profile essentially represents an inelastic mode shape by treating the structure as an equivalent elastic system. For structures with SSI effects, however, the appropriate displacement profile differs fundamentally, as higher-mode effects become more significant. Consequently, a modified expression for the displacement profile is required. The original formulation inherently assumes that the elastic first-mode shape is approximately linear with height, a premise based solely on elastic behavior. To develop a modified profile, the median displacement profiles obtained from the RC frames with SSI effects (Figs. 20 to 24) were combined. A machine learning (ML)-based curve-fitting procedure [12] was implemented in MATLAB to derive an enhanced displacement profile equation for an n-story frame with SSI effects. Indeed, a supervised machine learning model was developed to predict the seismic displacement distribution of RC frames incorporating SSI effects. The model is trained on a dataset derived from median nonlinear time-history analysis results of frame configurations subjected to seven scaled ground motions on two soil types. The output is the normalized peak inter-story displacement profile.

$$\Delta_{i.RC\_SSI} = C_1\theta_c\left(\frac{H_i}{H_n}\right)\left(1-\frac{1}{C_2}\left(\frac{H_i}{H_n}\right)\right) \quad . \qquad n \le 6$$
$$\Delta_{i.RC\_SSI} = C_3\theta_c\left(\frac{H_i}{H_n}\right)\left(1-\frac{1}{C_4}\left(\frac{H_i}{H_n}\right)+\frac{1}{C_5}\left(\frac{H_i}{H_n}\right)^2\right) \quad . \qquad 6 < n \le 12 \tag{51}$$
$$\Delta_{i.RC\_SSI} = C_6\theta_c\left(\frac{H_i}{H_n}\right)\left(1+\frac{1}{C_7}\left(\frac{H_i}{H_n}\right)-\frac{1}{C_8}\left(\frac{H_i}{H_n}\right)^2\right) \quad . \qquad n > 12$$

Table 7. Coefficients of Eq. 51.

The RC frame with SSI Effect	C_1	C_2	C_3	C_4	C_5	C_6	C_7	C_8
Coefficients	13.3	2.6	24.0	2.8	32.0	42.5	4.7	3.3

The coefficients for Eq. 51 are provided in Table 7. Figs. 25 to 29 compare the displacement response profiles calculated using Eq. 12 and the proposed Eq. 51 against the median response profiles from the NTHA of RC frames with SSI effects. In these figures, the horizontal axis represents the displacement from the NTHA, while the vertical axis represents the displacement calculated from the equations. For clarity, results from Eq. 12 are marked with red triangles, and results from the proposed Eq. 51 are marked with blue squares. A 1:1 line (error estimation line) is also plotted; points closer to this line indicate a more accurate prediction from the corresponding equation. As shown in Fig. 25, Eq. 12 provides a reasonable estimate for the three-story frame, as its results align more closely with the 1:1 line than those of Eq. 51. However, for the six-story frame (Fig. 26), the proposed Eq. 51 yields a better prediction. This improved accuracy is attributed to the increasing influence of SSI effects, which amplify higher-mode responses. In general, as the number of stories increases, SSI effects more significantly alter the fundamental vibration mode through higher-mode participation. Consequently, unlike the proposed Eq. 51, Eq. 12 becomes increasingly inaccurate for taller frames due to its inability to account for these effects, as demonstrated for the 9-, 12-, and 15-story frames in Figs. 27, 28, and 29, respectively. Furthermore, the coefficient of determination (R^2) for the proposed equation, presented in Table 8, confirms that Eq. 55 accurately predicts displacements for RC frames with SSI effects. These results validate that the proposed Eq. 55 is a suitable replacement for Eq. 12 for predicting the displacement of RC frames incorporating SSI.

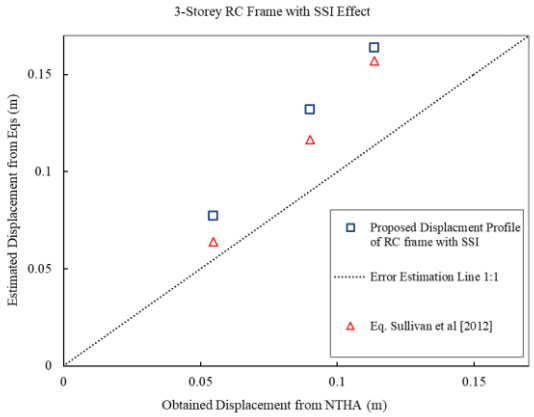

Fig. 25. Comparison of NTHA results with displacement profiles estimated by Sullivan et al. [7] (Eq. 12) and the proposed Eq. 51 for the 3-story RC frame with SSI effects.

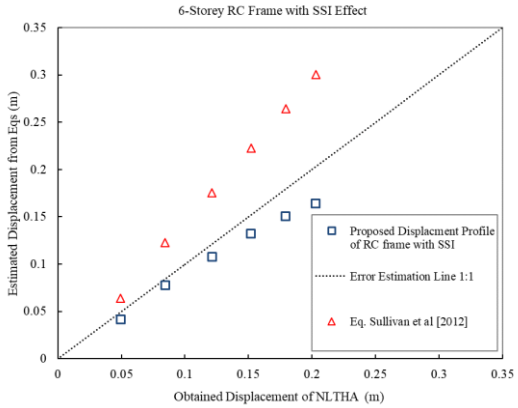

Fig. 26. Comparison of NTHA results with displacement profiles estimated by Sullivan et al. [7] (Eq. 12) and the proposed Eq.51 for the 6-story RC frame with SSI effects.

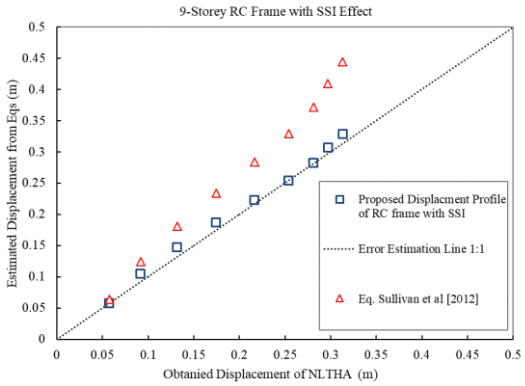

Fig. 27. Comparison of NTHA results with displacement profiles estimated by Sullivan et al. [7] (Eq. 12) and the proposed Eq. 51 for the 9-story RC frame with SSI effects.

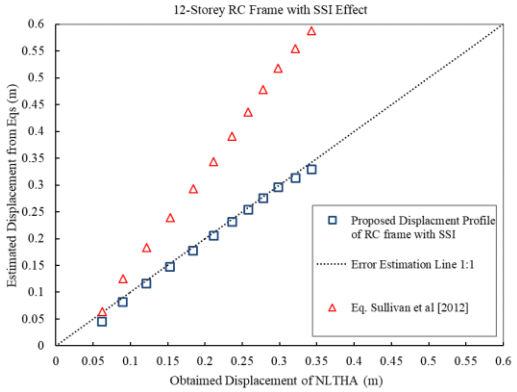

Fig. 28. Comparison of NTHA results with displacement profiles estimated by Sullivan et al. [7] (Eq. 12) and the proposed Eq. 51 for the 12-story RC frame with SSI effects.

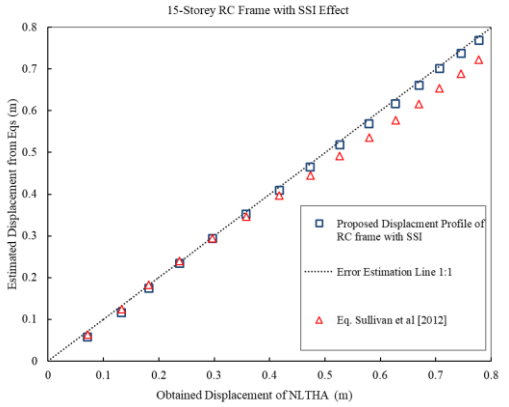

Fig. 29. Comparison of NTHA results with displacement profiles estimated by Sullivan et al. [7] (Eq. 12) and the proposed Eq. 51 for the 15-story RC frame with SSI effects.

Table 8. Coefficient of determination R2 of the proposed equation.

Proposed Equation	ML-Based formula for displacement prediction		
	Eq. 51 $n \leq 6$	**Eq. 51** $6 < n \leq 12$	**Eq. 51** $n > 12$
R^2 (%)	82	98	99

7. Summary and conclusion

This study proposes a novel Wavelet Transform-based Machine Learning Method (WTMLM) for the seismic design of reinforced concrete (RC) frames, explicitly incorporating soil-structure interaction (SSI) effects. The methodology introduces an equivalent three-degree-of-freedom (3DOF) system, solving the dynamic equilibrium equations to account for SSI. A new wavelet transform technique was developed to generate equivalent pulse-type excitation models. Consequently, new equations for demand displacement and stiffness were formulated, along with a novel design displacement profile capable of predicting the higher-mode amplifications induced by SSI. To validate the proposed method, five RC frames (3, 6, 9, 12, and 15 stories) were designed for a repairable damage performance level and subsequently analyzed using nonlinear time-history analysis (NTHA) under seven scaled earthquake records. The results, based on an evaluation of displacement and inter-story drift ratio profiles, are summarized as

follows:

- The proposed wavelet transform method effectively generates pulse-type functions by directly processing the primary earthquake acceleration while preserving the fundamental design frequencies. This approach is more practical than previous velocity-based methods, which often retain non-essential frequency content.
- The shear beam SSI model outperforms the cone model due to its detailed multi-layered representation of soil, which provides a more realistic basis for the design process.
- The NTHA results confirm that all RC frames designed using the WTMLM, except the 15-story frame, satisfied the 2% inter-story drift limit for the repairable damage performance level, demonstrating the method's success for low- to mid-rise structures with SSI.
- The drift profile of the 15-story frame with SSI exceeded the repairable limit, particularly between the 6th and 10th stories. This indicates that the higher mode effect coefficient may require modification to account for intensified higher-mode effects in taller structures, a subject for future research.
- For the 15-story frame with SSI, the NTHA results indicate that while the average drift in some stories exceeded the repairable limit (2%), it remained below the life safety limit (2.5%), thus still meeting code requirements.
- The results confirm that the proposed ML-based formula is a suitable and more accurate replacement for the available equation in the design of RC frames with SSI effects. Future work should focus on refining this profile for a broader range of structural configurations and soil parameters.

A key limitation of the current model is the exclusion of the foundation's rocking degree of freedom. This assumption is valid for the investigated regular RC structures but may require extension for taller buildings or softer soil conditions where rocking becomes a dominant response mechanism. Additionally, the validation is limited to regular RC frames on two-layer stiff soil profiles. Future research will focus on enriching the WTMLM framework by integrating rotational soil springs and exploring its applicability to structures founded on softer soils and taller building configurations.

Statements & Declarations

Author contributions

Sina Farahani: Investigation, Formal analysis, Data curation, Software, Writing - Original Draft.

Funding

The authors received no financial support for the research, authorship, and/or publication of this article.

Data availability

The data presented in this study will be available on request from the corresponding author.

Declarations

The authors declare no conflict of interest.

References

[1] American Society of Civil Engineers (ASCE). ASCE/SEI 7-16: Minimum Design Loads and Associated Criteria for Buildings and Other Structures. Reston (VA): ASCE; 2017.

[2] British Standards Institution. CEN EN 1998-1: Eurocode 8: Design of structures for earthquake resistance. Ispra (IT): EN; 1998.

[3] Building and Housing Research Center. Standard No. 2800: Iranian code of practice for seismic resistant design of buildings. Tehran (IR): 2800; 2015.

[4] Farahani, S., Akhaveissy, A. H., Damkilde, L. Towards a modified displacement-based seismic design of braced reinforced concrete frame structures considering soil structure interaction. Structures, 2025; 75: 108443. doi:10.1016/j.istruc.2025.108443.

[5] Priestley, M., Calvi, G., Kowalsky, M. Displacement-based seismic design of structures. 1st ed. Rome (IT): IUSS Press; 2007. doi:10.1002/EQE.807.

[6] Sullivan, T. J. Highlighting Differences between Force-Based and Displacement-Based Design Solutions for Reinforced Concrete Frame Structures. Structural Engineering International, 2013; 23: 122-131. doi:10.2749/101686613X13439149156958.

[7] Sullivan, T. J., Priestley, M. J. N., Calvi, G. M. A Model Code for the Displacement-Based Seismic Design of Structures. 1st ed. Rome (IT): IUSS Press; 2012.

[8] Chopra, A. K. Dynamics of structures: theory and applications to earthquake engineering. 1st ed. Prentice Hall (NJ): Upper Saddle River; 2007.

[9] Nazarimofrad, E., Farahani, S., Zahrai, S. M. Multiobjective optimal placement of active tendons to control irregular multistory buildings with soil–structure interaction. The Structural Design of Tall and Special Buildings, 2019; 28: e1581. doi:10.1002/tal.1581.

[10] Imam, M. H., Mohiuddin, M., Shuman, N. M., Oyshi, T. I., Debnath, B., Liham, M. I. M. H. Prediction of seismic performance of steel frame structures: A machine learning approach. Structures, 2024; 69: 107547. doi:10.1016/j.istruc.2024.107547.

[11] Demir, A., Sahin, E. K., Demir, S. Advanced tree-based machine learning methods for predicting the seismic response of regular and irregular RC frames. Structures, 2024; 64: 106524. doi:10.1016/j.istruc.2024.106524.

[12] Farahani, S., Barari, A. A simplified procedure for the prediction of liquefaction-induced settlement of offshore wind turbines supported by suction caisson foundation based on effective stress analyses and an ML-based group method of data handling. Earthquake Engineering & Structural Dynamics, 2023; 52: 5072-5098. doi:10.1002/eqe.4000.

[13] Salajegheh, E., Heidari, A., Saryazdi, S. Optimum design of structures against earthquake by discrete wavelet transform. International Journal for Numerical Methods in Engineering, 2005; 62: 2178-2192. doi:10.1002/nme.1279.

[14] Kamgar, R., Tavakoli, R., Rahgozar, P., Jankowski, R. Application of discrete wavelet transform in seismic nonlinear analysis of soil–structure interaction problems. Earthquake Spectra, 2021; 37: 1980-2012. doi:10.1177/8755293020988027.

[15] Dadkhah, M., Kamgar, R., Heidarzadeh, H. Reducing the Cost of Calculations for Incremental Dynamic Analysis of Building Structures Using the Discrete Wavelet Transform. Journal of Earthquake Engineering, 2022; 26: 3317-3342. doi:10.1080/13632469.2020.1798830.

[16] Kamgar, R., Dadkhah, M., Naderpour, H. Earthquake-induced nonlinear dynamic response assessment of structures in terms of discrete wavelet transform. Structures, 2022; 39: 821-847. doi:10.1016/j.istruc.2022.03.060.

[17] Yang, J., Li, F., Zhou, J., Zhang, Y., Li, P., Henry, R. S. Experimental Investigation of Seismic Damage in RC Frame Structures With Soil-Structure Interaction Using Wavelet Packet Transformation. Earthquake Engineering and Resilience, 2025; 4: 379-399. doi:10.1002/eer2.70018.

[18] Zhang, H., Wang, L., Shi, W. Seismic intelligent retrofitting of aging steel structure using semi-active TMD with LSTM prediction and wavelet transform combined algorithm. Thin-Walled Structures, 2025; 214: 113431. doi:10.1016/j.tws.2025.113431.

[19] Asgari, A., Bagheripour, M. H. Earthquake Response Analysis of Soil Layers Using HFTD Approach. Soil Dynamics and Earthquake Engineering. 2012. p. 320-325. doi:10.1061/41102(375)39.

[20] Akbarzadeh, M. R., Naeim, B., Asgari, A., Estekanchi, H. E. Framework for multi-hazard parameterized fragility based uncertainty quantification and sensitivity analysis of offshore wind turbines. Soil Dynamics and Earthquake Engineering, 2026; 201: 109963. doi:10.1016/j.soildyn.2025.109963.

[21] Asgari, A., Ranjbar, F., Bagheri, M. Seismic resilience of pile groups to lateral spreading in liquefiable soils: 3D parallel finite element modeling. Structures, 2025; 74: 108578. doi:10.1016/j.istruc.2025.108578.

[22] Asgari, A., Ahmadtabar Sorkhi, S. F. Wind turbine performance under multi-hazard loads: Wave, wind, and earthquake effects on liquefiable soil. Results in Engineering, 2025; 26: 104647. doi:10.1016/j.rineng.2025.104647.

[23] Idriss Izzat, M., Seed, H. B. Seismic Response of Horizontal Soil Layers. Journal of the Soil Mechanics and Foundations Division, 1968; 94: 1003-1031. doi:10.1061/JSFEAQ.0001163.

[24] Federal Emergency Management Agency (FEMA). Improvement of nonlinear static seismic analysis procedures. Washington, D.C. (US): FEMA; 2005.

[25] Lu, Y., Hajirasouliha, I., Marshall, A. M. An improved replacement oscillator approach for soil-structure interaction analysis considering soft soils. Engineering Structures, 2018; 167: 26-38. doi:10.1016/j.engstruct.2018.04.005.

[26] Agrawal, A. K., He, W. L. A closed-form approximation of near-fault ground motion pulses for flexible structures. In: Engineering Mechanics: Proceedings of the 11th Conference; 1996 May 19-22; Fort Lauderdale, Florida. p. 11-24.

[27] Makris, N., Black, C. J. Dimensional Analysis of Inelastic Structures Subjected to Near Fault Ground Motions. Berkeley (CA): Earthquake Engineering Research Center, University of California; 2003. Report No.: UCB/EERC 2003-05.

[28] Amiri, J. V., Davoodi, M. R., Sahafi, A. Simulation of Near-Fault Ground Motions With Equivalent Pulses & Compare Their Effects on MRF Structures. In: Proceedings of the 14th World Conference on Earthquake Engineering; 2008 Oct 12-17; Beijing, China. p. 1-19.

[29] Misiti M, M. Y., Oppenheim G, Poggi JM Wavelet toolbox reference. 1st ed. Natick (MA): The MathWorks; 213.

[30] American Concrete Institute. ACI 318-14: Building code requirements for structural concrete (ACI 318-14). Farmington Hills (MI): ACI; 2014.

[31] Khampanit, A., Leelataviwat, S., Kochanin, J., Warnitchai, P. Energy-based seismic strengthening design of non-ductile reinforced concrete frames using buckling-restrained braces. Engineering Structures, 2014; 81: 110-122. doi:10.1016/j.engstruct.2014.09.033.